Neuron

Article

Ethological learning during the critical period resets synaptic setpoints in mouse binocular visual cortex

Graphical abstract

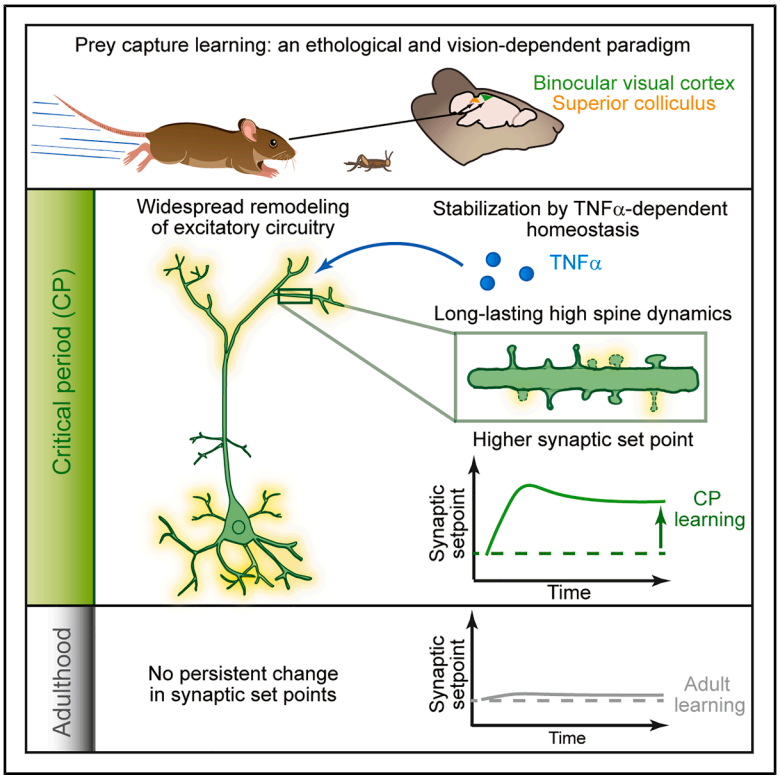

Highlights

- Ethological, visual learning (prey capture) improves visual speed discrimination
- Learning persistently shifts excitatory synaptic setpoints and dynamics
- Such remodeling only occurs during the visual critical period but not in adults
- Homeostatic mechanisms stabilize the structural, functional, and behavioral changes

Authors

Diane Bissen, Brian A. Cary, Amanda Zhang, Wei Wen, Kurt A. Sailor, Stephen D. Van Hooser, Gina G. Turrigiano

Correspondence

turrigiano@brandeis.edu

In brief

Bissen et al. show that prey capture learning profoundly reshapes visual cortical circuitry and function during developmental critical periods, but not in adulthood. These learning-induced structural and functional changes are stabilized by homeostatic mechanisms that reset synaptic setpoints, thus facilitating learning and retention of this naturalistic, vision-dependent behavior.

Bissen et al., 2026, Neuron *114*, 1–20
December 9, 2026
https://doi.org/10.1016/j.neuron.2026.06.016

CellPress

Please cite this article in press as: Bissen et al., Ethological learning during the critical period resets synaptic setpoints in mouse binocular visual cortex, Neuron (2026), https://doi.org/10.1016/j.neuron.2026.06.016

Neuron

CellPress
OPEN ACCESS

Article

Ethological learning during the critical period resets synaptic setpoints in mouse binocular visual cortex

Diane Bissen,[1] Brian A. Cary,[1] Amanda Zhang,[1] Wei Wen,[1] Kurt A. Sailor,[2] Stephen D. Van Hooser,[1] and Gina G. Turrigiano[1,3,*]

[1]Department of Biology, Brandeis University, Waltham, MA 02453, USA
[2]Institut Pasteur, CNRS UMR 3571, Perception and Action Unit, F-75015, Paris, France
[3]Lead contact
*Correspondence: turrigiano@brandeis.edu
https://doi.org/10.1016/j.neuron.2026.06.016

SUMMARY

Critical periods are developmental windows that allow experience-dependent refinement of neuronal circuitry and function. While the consequences of sensory deprivation or alteration during the visual critical period have been well characterized, the impact of ethological experiences requiring active interaction with the sensory world is largely unexplored. Here, we use prey capture learning to assess structural and functional plasticity associated with visual learning in the primary visual cortex of critical-period mice. We show that prey capture learning supports improved temporal frequency discrimination and profoundly remodels visual circuitry by increasing spine turnover and moving spine density across the dendritic arbors of pyramidal neurons to new stable values. This widespread and persistent rewiring is absent in adults and supported by tumor necrosis factor α (TNF-α)-dependent homeostatic plasticity that contributes to behavioral improvement. Ethological critical period learning can thus co-opt homeostatic mechanisms to reset synaptic weight bounds to enable widespread synaptic remodeling to support improved visual function and behavior.

INTRODUCTION

During postnatal development, young mammals improve perceptual and motor skills by interacting with the world. While brains remain adaptable throughout life, in sensory and higher-association areas, experience-dependent plasticity is at its peak during "critical periods" (CPs)—short windows in postnatal development when neuronal circuitry is particularly susceptible to refinement by experience.[1–3] In the visual system, CP plasticity is believed to adjust brain circuitry to match the visual world to improve active sensory processing and thus survival.[1–3] However, establishing a role for CP plasticity in visual system improvement has been hampered by the near-exclusive use of deprivation or overstimulation paradigms, which distort normal function by altering the development and/or maintenance of visual receptive field (RF) properties,[4–15] partly through changes in primary visual cortical (V1) circuitry.[16–21] While these paradigms have been tremendously useful for defining the landscape of CP plasticity, they may provide limited insight into how ethological experiences requiring active interaction with the environment tune visual circuitry during the CP to improve function. To address this gap, we use a vision-dependent behavior—prey capture learning—to ask whether naturalistic visual learning drives CP plasticity to improve function.

Learning is proposed to rewire brain circuitry throughout life to incorporate and stabilize behaviorally relevant connections to improve function and ensure optimal behavioral outcomes.[22,23] In the adult cortex, this rewiring generally operates within the constraints of a globally stable network, where neuronal firing rates[24–30] and the majority of dendritic spines[31–35] are stable over long periods of time: while learning can rapidly increase spine formation, this is quickly balanced by the elimination of extraneous connections, thus adjusting connectivity with little sustained impact on spine density.[36–39] Furthermore, the trade-off between spine number and size during Hebbian plasticity in the adult hippocampus suggests that total spine volume is conserved, possibly because the resources needed for spine maintenance are homeostatically limiting.[40] Together, these findings suggest that adult cortical spine density is regulated around a stable setpoint, while spine turnover enables rewiring during learning through loss and gain of specific connections.[41–43] Intriguingly, prolonged exposure to enriched environments (EEs) can enhance spine density and dynamics,[44–47] but because this enhancement does not persist beyond return to standard housing,[44] it is not clear whether enrichment can persistently modify synaptic setpoints or exactly which features drive these changes. We recently found that prey capture learning during the CP can reset firing rate setpoints in V1,[48]

Please cite this article in press as: Bissen et al., Ethological learning during the critical period resets synaptic setpoints in mouse binocular visual cortex, Neuron (2026), https://doi.org/10.1016/j.neuron.2026.06.016

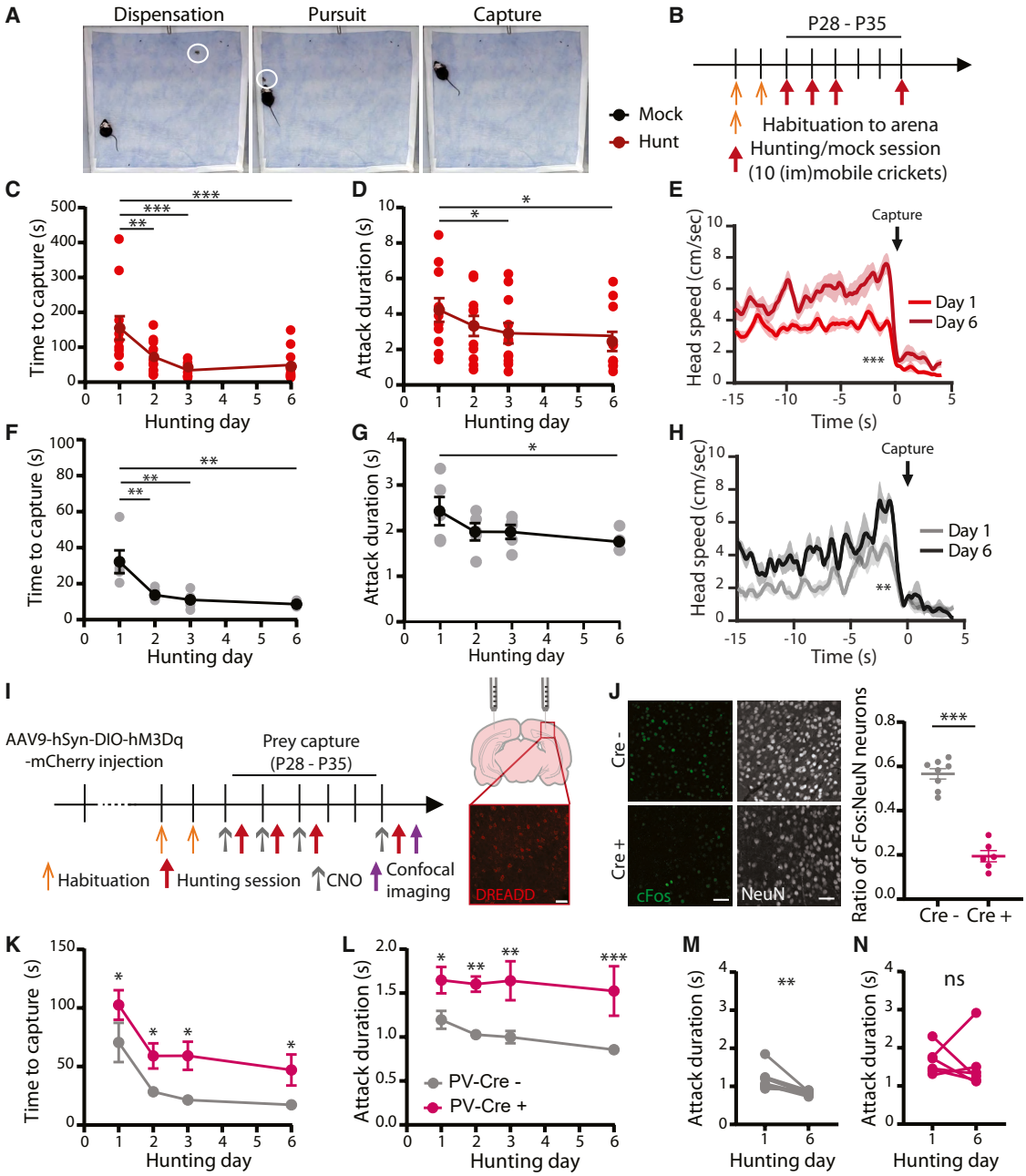

Figure 1. Efficient and persistent prey capture learning in CP mice depends on V1

(A) Hunting arena with CP mouse and cricket (white circle) during cricket dispensation (left), pursuit (middle), and capture (right).

(B) Experimental timeline of the prey capture learning paradigm.

(C and F) Average time to capture (s) for each hunting (C) or mock (F) session (10 crickets). Here and below, light dots represent individual animal averages, and dark dots represent across-animal average (mean ± SEM). For (C)–(H), *N* = 8 mice (hunting) and 5 mice (mock).

(D and G) Same as (C) and (F) but for average attack duration (s) for each hunting (D) or mock (G) session.

(E and H) Average head speed (cm/s) centered on capture (t = 0 s) for all hunts during the first (day 1, light lines) and the last (day 6, dark lines) hunting (E) or mock (H) session.

(I) Experimental timeline for DREADD-mediated V1 inhibition during prey capture learning. Inset: PV interneurons expressing excitatory DREADDs (labeled with mCherry). Scale bar, 50μm.

(J) Left, representative images of V1 from PV-Cre^{-} (top) or PV-Cre^{+} (bottom) mouse, labeled for cFos (green) and NeuN (white). Right, fraction of NeuN^{+} neurons that are also cFos^{+} in littermates with (Cre^{+}) or without (Cre^{-}) V1 inhibition (mean ± SEM). Scale bar, 50 μm. For (I)–(N), *N* = 8 PV-Cre^{-} mice and 6 PV-Cre^{+} mice.

(legend continued on next page)

Please cite this article in press as: Bissen et al., Ethological learning during the critical period resets synaptic setpoints in mouse binocular visual cortex, Neuron (2026), https://doi.org/10.1016/j.neuron.2026.06.016

raising the possibility that homeostatic brakes on synapse density might also be persistently modifiable by active vision-dependent learning during the visual system CP.

Prey capture learning is an ideal paradigm for probing learning-induced plasticity during the visual CP.[49,50] Rodents are opportunistic predators in the wild,[51] and this instinctive behavior is present in laboratory animals.[49,50,52–54] While the predatory drive is innate, successful hunting is a skilled behavior that mice rapidly learn through practice.[49,50,52–54] Importantly, prey capture is vision dependent,[50] but although the contributions of different retinal and collicular cell types have been characterized,[53,54] little is known about the mechanisms or locus of plasticity in either adult or CP mice. Here, we set out to determine whether active visual learning can modify V1 circuitry to improve function and whether this is mediated through CP-specific plasticity.

We designed a prey capture learning paradigm in CP mice to investigate visual learning-induced functional and structural plasticity in binocular V1 (V1b), using *in vivo* two-photon spine or calcium imaging in awake, head-fixed mice and large-scale, high-resolution confocal microscopy. Comparing hunting with a "mock hunting" paradigm (akin to foraging) enabled us to differentiate between the effects of mild enrichment and active visual learning. We first demonstrated that hunting in CP mice, as for CP rats,[48] relies on V1. We then assessed RF properties in V1b and found that prey capture learning enhanced the discriminability of visual stimuli moving at different speeds, to a degree directly correlated with hunting proficiency. Learning was accompanied by a persistent and dramatic increase in spine density and dynamics in L5 pyramidal neurons, with no parallel increase in inhibition, thereby effectively shifting V1b into a highly dynamic state centered around a new, elevated setpoint for spine density. Intriguingly, widefield cells of the superficial superior colliculus (sSC) were also remodeled in a V1-independent manner, suggesting that hunting drives parallel changes in cortical and subcortical visual pathways. Finally, spine density in V1b was increased onto CP L2/3 and L5 pyramidal neurons but unaffected in adults, indicating that this plasticity is CP-specific. Finally, blocking tumor necrosis factor α (TNF-α) signaling (which prevents homeostatic increases in synaptic strength in V1[55,56]) after initial learning prevented both structural and functional correlates of learning and impaired the retention of hunting skills. Together, our results show that ethological learning during the CP profoundly remodels visual circuitry and function, improves vision-dependent behavior, and moves excitatory synaptic setpoints to new, higher values.

RESULTS

Efficient prey capture learning in critical-period mice depends on V1

To investigate the plasticity mechanisms within V1b that mediate the acquisition and retention of hunting skills, we devised a hunting paradigm comprised of the habituation of CP mice to the hunting arena for 2 days, followed by prey capture learning with one hunting session (10 live crickets) per day for three consecutive days, a 2-day break, and a final hunting session to assess skill retention (Figures 1A and 1B). Control (mock) animals followed the exact same paradigm but received 10 immobilized crickets in "mock hunting" sessions, akin to foraging.

Consistent with previous results,[49] hunting mice showed a rapid and dramatic decrease in the time from cricket release to capture (time to capture) that persisted until the last hunting session (Figures 1C and S1A; effect size for Figure 1C, day 6, calculated as Hedge' g: 1.1870; see Table S1 for statistical tests and effect sizes). Importantly, mice became faster at detecting crickets, initiating pursuit (latency to attack; Figure S1B), and capturing them (attack duration; Figure 1D [Hedge's g, day 6: 0.6943], S1C), indicating an improvement in hunting efficiency. Using DeepLabCut[57] for finer behavioral analysis revealed that reduced time to capture was associated with a ∼50% speed increase during the final (successful) attack (Figure S1D) and a terminal speed burst as mice approach and grasp the cricket (Figure 1E).

Intriguingly, mock mice also captured immobilized crickets significantly faster over time, and the time course of improvement was strikingly similar to that of hunting mice (Figures 1F, 1G, and S1E; Hedge's g for day 6: [F] 2.1069, [G] 1.1825). While the average "attack" speed did not increase significantly (Figure S1F), mock animals also developed a final speed burst prior to cricket "capture" (Figure 1H). Hunting and mock mice had comparable average speeds during inter-cricket intervals, suggesting a similar exploratory behavior (Figure S1G), and captured and consumed the same number of crickets (Figure S1H). Finally, tail angle changed at cricket capture: tails were straight during pursuit, reminiscent of tail use by predators for stabilization and direction changes during pursuit,[58] and curved (suggesting relaxation) at capture for both hunting and mock mice (Figures S1I and S1J). Taken together, these data show that hunting and mock mice are similarly motivated to explore the arena and search for food rewards. Our paradigm thus allows us to focus on changes driven by learning of a complex visuo-motor task in which mice must track and capture moving prey.

Prey capture learning is a complex sensorimotor task relying on several brain regions.[59] To assess whether it requires V1, we chemogenetically inactivated V1 during learning by expressing a cre-dependent excitatory designer receptor activated by designer drug (DREADD)[60] bilaterally in V1b of parvalbumin (PV)-Cre mice, then administering the DREADD ligand clozapine N-oxide (CNO) 45 min before each hunting session to activate PV inhibitory neurons and silence V1 (Figure 1I). Quantification of cFos expression in V1 pyramidal neurons (using NeuN as a pyramidal neuron marker[61]) at the end of the paradigm confirmed that this strategy efficiently silenced V1 in juvenile mice as it

(K and L) Behavior from animals in (J). Average time to capture (K) or attack duration (L) (s). Data presented as mean ± SEM per genotype. Asterisks show statistical comparisons between genotypes per session.

(M and N) Average attack duration (s) for each PV-Cre$^-$ (M) or PV-Cre$^+$ (N) mouse on day 1 and day 6.

*$p < 0.05$, **$p < 0.01$, and ***$p < 0.001$. For statistical tests, exact p values and effect sizes for all figures, see Table S1.

See Figure S1.

Please cite this article in press as: Bissen et al., Ethological learning during the critical period resets synaptic setpoints in mouse binocular visual cortex, Neuron (2026), https://doi.org/10.1016/j.neuron.2026.06.016

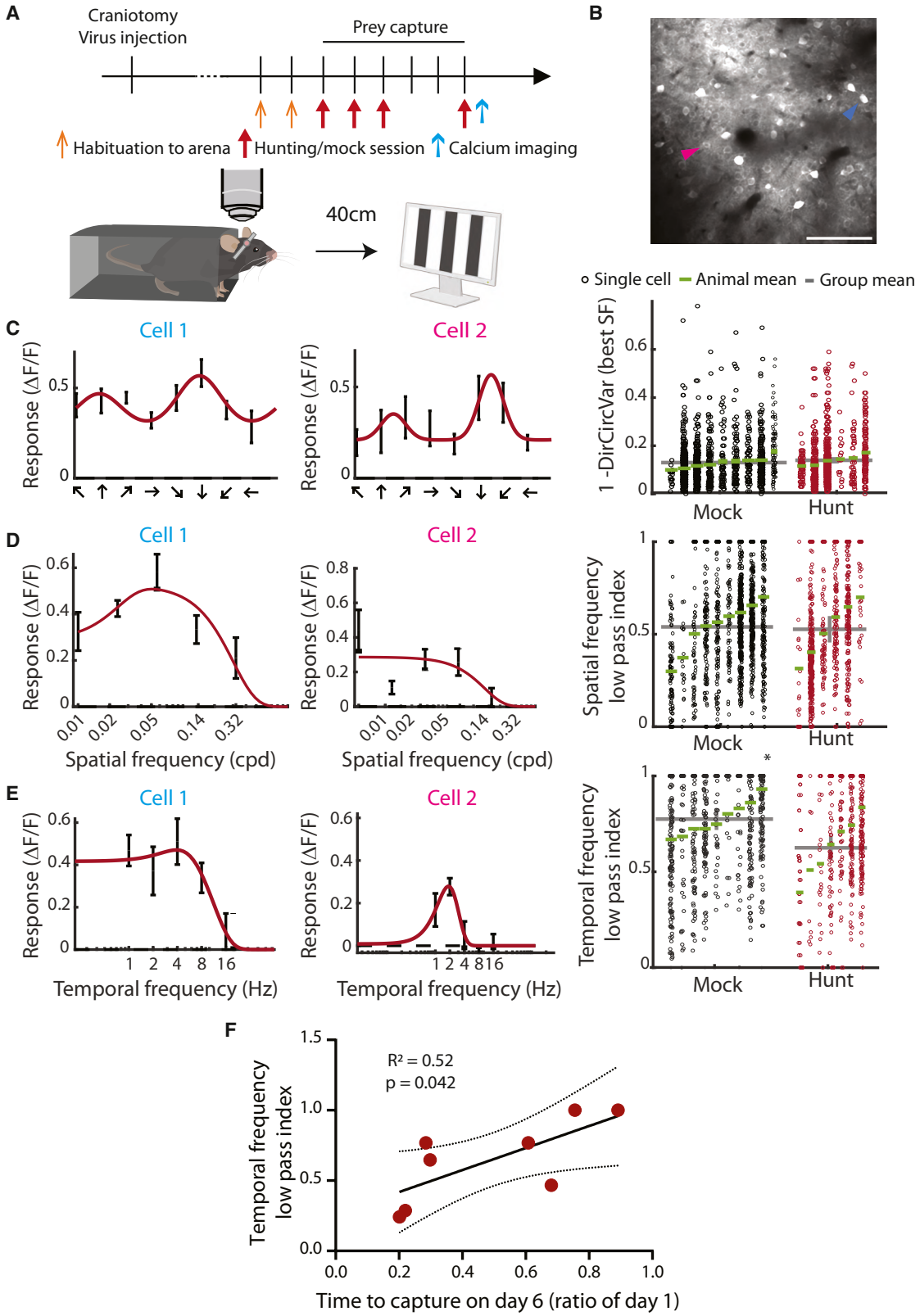

(legend on next page)

Please cite this article in press as: Bissen et al., Ethological learning during the critical period resets synaptic setpoints in mouse binocular visual cortex, Neuron (2026), https://doi.org/10.1016/j.neuron.2026.06.016

does in rats[48] (Figure 1J). While Cre$^-$ animals showed a significant improvement in performance as expected (Figures 1K–1M, S1K, and S1M), the performance of Cre$^+$ animals plateaued at a significantly worse level (Figure 1K) and was primarily driven by a decrease in latency to attack (Figures S1L and S1N), with no decrease in attack duration (Figure 1N). These results indicate that V1 contributes to prey capture learning in CP mice, raising the question of whether this learning drives plastic changes within the V1 microcircuit.

Prey capture learning improves speed discrimination

RF properties can be altered by sensory deprivation during the CP,[9,10,14,15] but it is unclear whether they can be improved by visual learning during this developmental window. Therefore, we investigated whether prey capture learning modifies RF tuning during the CP. Here and below, we focused on binocular V1 (V1b), as adult mice are known to use binocular vision for hunting.[50,52,53] We expressed the calcium indicator GCaMP6s to label V1b L2/3 neurons, ran them through our learning paradigm (Figure 2A), and then performed *in vivo* two-photon calcium imaging in awake, head-fixed mice to assess common RF properties using grating stimuli of varying directions, contrasts, and temporal or spatial frequencies (Figures 2A and 2B). We then calculated tuning curves for individual neurons and ran a nested analysis (see STAR Methods) to compare the distribution of all responses (weighted by animal) between hunting and mock mice.

Most RFs tested were not affected by hunting. We found no significant differences in contrast sensitivity (Figure S2B), direction selectivity (Figure 2C), orientation selectivity (Figure S2C), or ocular dominance index (Figure S2D). The preferred spatial frequency (Figure S2E) and low-pass index for spatial frequency (Figure 2D) were also unchanged. By contrast, temporal frequency (TF) selectivity was significantly improved by hunting (Figure 2E; Cohen's d, −0.5303). While the preferred TF was similar between hunting and mock mice (Figure S2F), fewer neurons in hunting mice acted as low-pass temporal filters (Figure 2E, cell 1), and more had sharp TF tuning (Figure 2E, cell 2), as indicated by a drop in the TF low-pass index (Figure 2E, right panel). Behaviorally speaking, this suggests that prey capture learning leads to an improvement of the ability to discriminate between visual stimuli moving at different speeds. If this improvement contributes to successful hunting, then better hunters should have better TF discrimination (i.e., a lower low-pass index). Indeed, there was a strong correlation between the TF low-pass index and improvement in performance (expressed as the ratio of time to cricket capture on day 6 and day 1; Figure 2F).

Prey capture learning induces a persistent increase in excitatory drive to L5 pyramidal dendrites

Whether learning ethologically relevant visual skills can drive structural changes in V1, either in CP or adults, is unknown. Since prey capture learning can modify response properties in V1b (Figure 2), we asked whether it also leads to morphological adaptations. To test this, we ran CP mice from the Thy1-YFP line H[62] through our prey capture paradigm and perfused them after the first (day 1) or last (day 6) hunting session to capture changes associated with the acquisition or retention of learned skills (Figure 3A). We then performed large-scale, high-resolution imaging and 3D reconstruction of yellow fluorescent protein (YFP)-expressing pyramidal neurons to quantify spine density changes (as a proxy for excitatory synapse number) (Figure 3B; Video S1) and spine head diameter changes (correlated with postsynaptic strength) (Figure 3C)[63,64] across the entire dendritic arbor.

In L5 pyramidal neurons, spine density was already significantly increased in hunting compared with mock on day 1. A cumulative distribution function (CDF) of spine density across dendrites was significantly shifted rightward (Figure 3D; probability of superiority (PS), 0.6110), and a nested analysis revealed a significant increase in spine density in hunting neurons (Figure 3E; Cohen's d, 0.4170). By day 6, these changes were even more pronounced (Figures 3F and 3G; PS 0.6615, Cohen's d 0.6624) and accompanied by an increase in spine head size driven by a higher proportion of larger spines, as shown in the population CDF and an analysis by quintiles (Figures S3A–S3E; Cohen's d for top quintile, 0.5663). Prey capture learning thus increases total L5 spine volume (number and size). There was a similar increase in spine density, but not size, by day 6 in L2/3 pyramidal neurons, albeit with slower dynamics as no changes were apparent by day 1 (Figures S3F–S3K). These data suggest that prey capture learning-induced remodeling of V1b excitatory circuitry is widespread across cortical layers.

The rightward shift in the spine density CDFs (Figures 3D and 3F) suggests that this increase is widespread across the L5 pyramidal dendritic arbor. Since L5 apical, oblique, and basal dendrites receive inputs from distinct sources,[65,66] we analyzed these compartments separately (Figure 3B; see STAR Methods). We found an increase in spine density in apical and basal, but not oblique, dendrites from hunting mice

Figure 2. Prey capture learning improves speed discrimination

(A) Experimental timeline with *in vivo* imaging of RF properties in awake CP mice.

(B) Representative image of GCaMP6s$^+$ L2/3 neurons. Blue and pink arrowheads show cells 1 and 2 from (C)–(E). Scale bar, 100 μm.

(C) Left, middle: example direction tuning curves. Right: nested analysis for direction selectivity (measured as 1-DirCirVar, see STAR Methods) at the best spatial frequency (SF). n = 2,210 cells from 8 mice (mock) and 819 cells from 6 mice (hunting).

(D) Left, middle: example spatial tuning curves. Right: nested analysis for SF low-pass index (LPI, cycle per degree, cpd). n = 2,253 cells from 9 mice (mock) and 764 cells from 6 mice (hunting).

(E) Left, middle: example temporal tuning curves. Right: nested analysis for temporal frequency (TF) LPI (Hz). n = 1,686 cells from 9 mice (mock) and 628 cells from 7 mice (hunting).

(F) TF LPI as a function of time to capture on day 6 (as ratio of day 1). Red dots represent individual hunting animals (N = 8), the black line a simple linear regression fit, and the dotted lines the borders of the 95% confidence interval.

$^*p < 0.05$

See Figure S2 and Table S1. Figures 2, 3, 4, 5, 6, and 8: in all nested analysis graphs, each column shows all units (dendrites, spines, or responsive GCaMP6s$^+$ cells) for an animal or a neuron, with the random effects per animal or neuron shown in green and the group mean per condition shown as a gray bar.

Please cite this article in press as: Bissen et al., Ethological learning during the critical period resets synaptic setpoints in mouse binocular visual cortex, Neuron (2026), https://doi.org/10.1016/j.neuron.2026.06.016

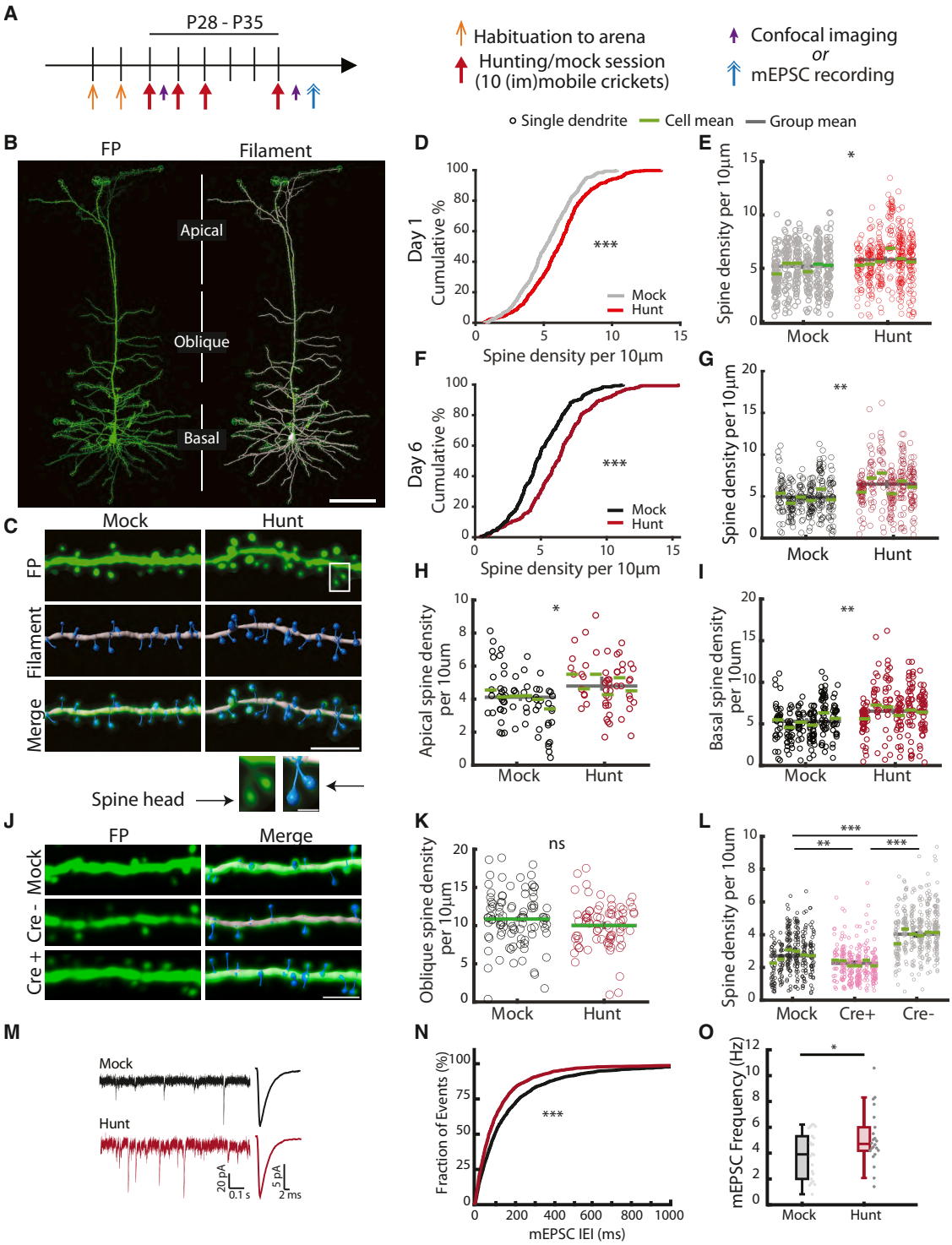

Figure 3. Prey capture learning induces a long-lasting increase in excitatory drive onto L5 pyramidal dendrites

(A) Experimental timeline with perfusion or by mEPSC recording.

(B) Representative images of an L5 pyramidal neuron (left) merged with its Imaris reconstructions (right), with apical, oblique, and basal compartments indicated. Scale bar, 100 µm.

(C) Top: representative images of a dendrite (top), its filament tracing (middle), and the merged picture (bottom) in a mock (left) or hunting (right) mouse. Scale bar, 5 µm. Bottom: magnification from the middle panel, white box. Scale bar, 1 µm.

(legend continued on next page)

Please cite this article in press as: Bissen et al., Ethological learning during the critical period resets synaptic setpoints in mouse binocular visual cortex, Neuron (2026), https://doi.org/10.1016/j.neuron.2026.06.016

(Figures 3H, 3I, and 3K). As oblique dendrites receive direct feedforward sensory input from the retinogeniculate pathway, while apical and basal trees receive recurrent and feedback connections,[65,66] these results strongly suggest that prey capture learning leads to a selective remodeling of feedback and recurrent connections onto L5 pyramidal neurons.

If visual drive remodels V1b to improve behavior during learning, then inactivating V1 during learning should prevent this rewiring. To test this, we reconstructed L5 pyramidal neurons from animals in which V1 was inactivated during learning (Figure 1K) and compared spine density and size in Cre$^+$ and Cre$^-$ hunting mice, relative to mock mice (PV-Cre × Thy1-YFP line H; Figure 3J). Consistent with our previous datasets, Cre$^-$ hunting mice had higher spine densities compared with mock mice. Strikingly, this increase was completely absent in Cre$^+$ mice (Figure 3L), indicating that spine plasticity requires V1 activation during hunting.

To test whether this increase in spine density results in functional changes in synaptic input, we measured miniature excitatory postsynaptic currents (mEPSCs) from Thy1$^+$ V1b L5 pyramidal neurons in acute slices prepared from hunting or mock mice (Figures 3M and S3L). Consistent with the widespread increase in spine density and more selective increase in spine head size, hunting mice showed a significantly higher mEPSC frequency (Figure 3N) and a correspondingly smaller inter-event interval (Figure 3O), with a small increase in mEPSC amplitude (significant only in the CDF, Figures S3M and S3N).

Taken together, these data show that prey capture learning induces a persistent and widespread increase in functional excitation onto L5 pyramidal neurons by enhanced long-range and local recurrent feedback connections.

Prey capture learning does not increase spine density onto L5 pyramidal neurons in adult hunters

Many forms of V1 plasticity are more pronounced during the CP than in adults,[1] and the impact of visual perceptual training on structural plasticity in adult V1 is unclear, since it has been reported to either increase[67] or decrease[68] spine density. To determine whether prey capture learning drives structural plasticity outside the CP, we ran young adult Thy1-YFP mice through our paradigm and quantified spine density on day 6 (Figures 4A and 4B). Time to capture in adults improved at a similar rate to juveniles for hunting (Figures 4C and S4A) and mock (Figures 4D and 4E) conditions. In contrast to CP mice, we found no differences in spine density or size in L5 (Figures 4F–4H and S4D) or L2/3 (Figures S4B, S4C, and S4E) pyramidal neurons between hunting and mock adult mice. These data strongly suggest that prey capture learning is mediated by distinct mechanisms in CP and adult mice.

Prey capture learning induces a V1-independent increase in spine density of widefield cells in the SC

In addition to V1 (Figure 1), subcortical visual pathways, especially the superficial SC,[53,69,70] are also important for prey capture behavior. A subset of widefield vertical (WF) cells, which mediate long-range prey detection and approach,[53] express YFP in Thy1-YFP mice. Since these are spiny neurons,[71,72] we measured spine density and size in these neurons, which revealed a large increase in spine density with no change in spine head size (Figure S5).

Since WF cells receive direct input from V1 L5 pyramidal neurons,[73] we wondered whether learning-dependent remodeling in sSC depends on activity in V1. To test this, we quantified WF spine density and size in PV-Cre x Thy1-YFP mice with V1 inhibited (Figures 5A and 5B; see Figure 1I). We found that spine density increased to the same extent in mice with (Cre$^-$) and without (Cre$^+$) V1 activity during hunting, indicating that V1 activity is not necessary to drive structural plasticity in sSC WF cells (Figures 5C–5G). Taken together, these data suggest that prey capture learning drives parallel plastic changes in cortical and subcortical visual structures.

Perisomatic and total dendritic inhibition onto L5 pyramidal neurons is unchanged in hunting mice

To investigate whether prey capture learning in CP mice drives structural changes in inhibition as well as excitation, we first examined PV-positive (PV$^+$) interneuron contacts, which provide strong perisomatic inhibition onto pyramidal neurons.[74,75] We labeled axonal PV+ interneuron boutons with Synaptotagmin 2 (Syt2) in Thy1+ hunting and mock mice (Figure 6A[76]), performed 3D reconstructions, and quantified the number and volume of Syt2$^+$ boutons onto L5 pyramidal somata (Figures S6A–S6H). This revealed no significant change in CDFs of Syt2$^+$ contact volume or in contact number (Figures 6C, 6D, and S6I), indicating that prey capture learning has little impact on perisomatic inhibition onto L5 pyramidal neurons.

PV interneurons also project onto other PV$^+$ neurons.[65] We thus investigated Syt2$^+$ boutons onto PV$^+$ somata in V1b L5 (Figure 6B) and found larger Syt2$^+$ contacts in hunting mice (Figures 6E and S6J). Since PV$^+$ soma size (Figures S6K and S6L) and PV-PV contact number (Figure 6F) remained unchanged in hunting mice, our results suggest an enlargement of existing PV-PV inhibitory connections rather than the establishment of new contacts.

(D and E) Cumulative distribution (D) or nested analysis (E) of spine density across all animals at day 1. n = 433 dendrites (mock) and 411 dendrites (hunting). (D–L) Each condition represents data from 6 neurons from 3–4 mice.
(F and G) Cumulative distribution (F) or nested analysis (G) of spine density across all animals at day 6. n = 268 dendrites (mock) and 272 dendrites (hunting).
(H, I, and K) Nested analysis of apical (H), basal (I), or oblique (K) spine density at day 6. (H) n = 67 dendrites (mock) and 53 dendrites (hunting). (I) n = 201 dendrites (mock) and 219 dendrites (hunting). (K) n = 93 dendrites (mock) and 78 dendrites (hunting).
(J) Representative images of dendrites (left) merged with their Imaris reconstructions (right) from mock, hunting Cre$^-$ and Cre$^+$ mice. Scale bar, 5 μm.
(L) Nested analysis of spine density in DREADD-injected mice. n = 293 dendrites (PV-Cre$^+$), 409 dendrites (PV-Cre$^-$), and 313 dendrites (mock).
(M) Representative traces of mEPSC recordings (left) and their average waveforms (right) from the indicated conditions.
(N) Cumulative distributions of mEPSC inter-event intervals (IEI). (N and O) n = 22 neurons from 3 animals per condition.
(O) Comparison of the mean (± SEM) mEPSC frequencies from hunting and mock mice.
*p < 0.05, **p < 0.01, and ***p < 0.001.
See Figure S3 and Table S1.

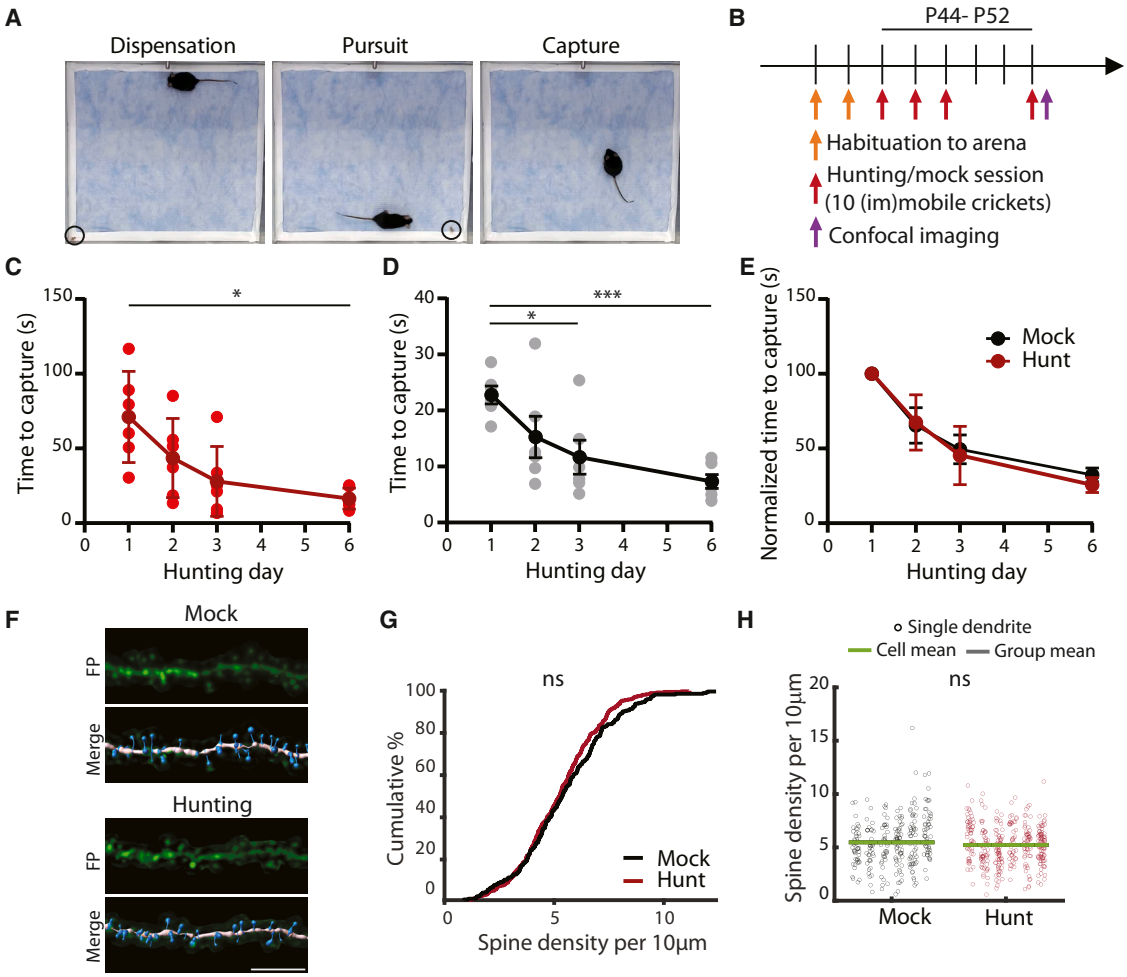

Figure 4. Prey capture learning does not increase spine density onto L5 pyramidal neurons in adult hunters

(A) Hunting arena with adult mouse and cricket (black circle) at cricket dispensation (left), pursuit (middle), and capture (right).

(B) Experimental timeline in adult mice.

(C and D) Average time to capture (s) for each hunting (C) or mock (D) session (10 crickets). Light dots represent individual animal averages, and dark dots represent across-animal averages (mean ± SEM). (C–E) $N = 6$ mice per condition.

(E) Average time to capture for each hunting or mock session, normalized to the average time to capture of day 1 (%).

(F) Representative images of dendrites (top) merged with their Imaris reconstructions (bottom) from mock (top) and hunting (bottom) mice. Scale bar, 5 µm.

(G and H) Cumulative distribution across all animals (G) and nested analysis (H) of spine density. $n = 282$ dendrites (mock) and 373 dendrites (hunting) from 6 neurons from 3 mice per condition.

$^{*}p < 0.05$ and $^{***}p < 0.001$.

See Figure S4 and Table S1.

Somatostatin (SST) interneurons provide a major source of dendritic inhibition.[74,75] We next immunolabeled against SST and vesicular GABA transporter (VGAT) and reconstructed SST and VGAT puncta in contact with L5 pyramidal YFP^{+} dendrites to quantify the density of total SST^{+}, total VGAT^{+}, and colocalized SST^{+}:VGAT^{+} puncta along apical or basal dendrites (Figure 6G). There was no change in apical puncta density (Figures S6M–S6O), and while learning had little effect on basal VGAT^{+} puncta density (Figure 6H), SST^{+} and colocalized SST^{+}:VGAT^{+} puncta density was significantly reduced (Figures 6I and S6P). This suggests either a downregulation of SST in SST synaptic terminals or a selective reduction in SST-mediated dendritic inhibition compensated by other inhibitory subclasses to maintain total dendritic inhibitory synapse density.

Together these results show that learning drives only modest structural remodeling of inhibition onto L5 pyramidal neurons. In particular, excitatory and inhibitory synapse density do not increase in parallel; rather, prey capture learning leads to a selective increase in excitatory input onto L5 pyramidal neurons.

Hunting persistently enhances spine turnover onto L5 pyramidal apical dendrites

The learning-induced increase in excitatory synapse number in CP mice could be due to enhanced synapse formation, reduced

Please cite this article in press as: Bissen et al., Ethological learning during the critical period resets synaptic setpoints in mouse binocular visual cortex, Neuron (2026), https://doi.org/10.1016/j.neuron.2026.06.016

CellPress
OPEN ACCESS

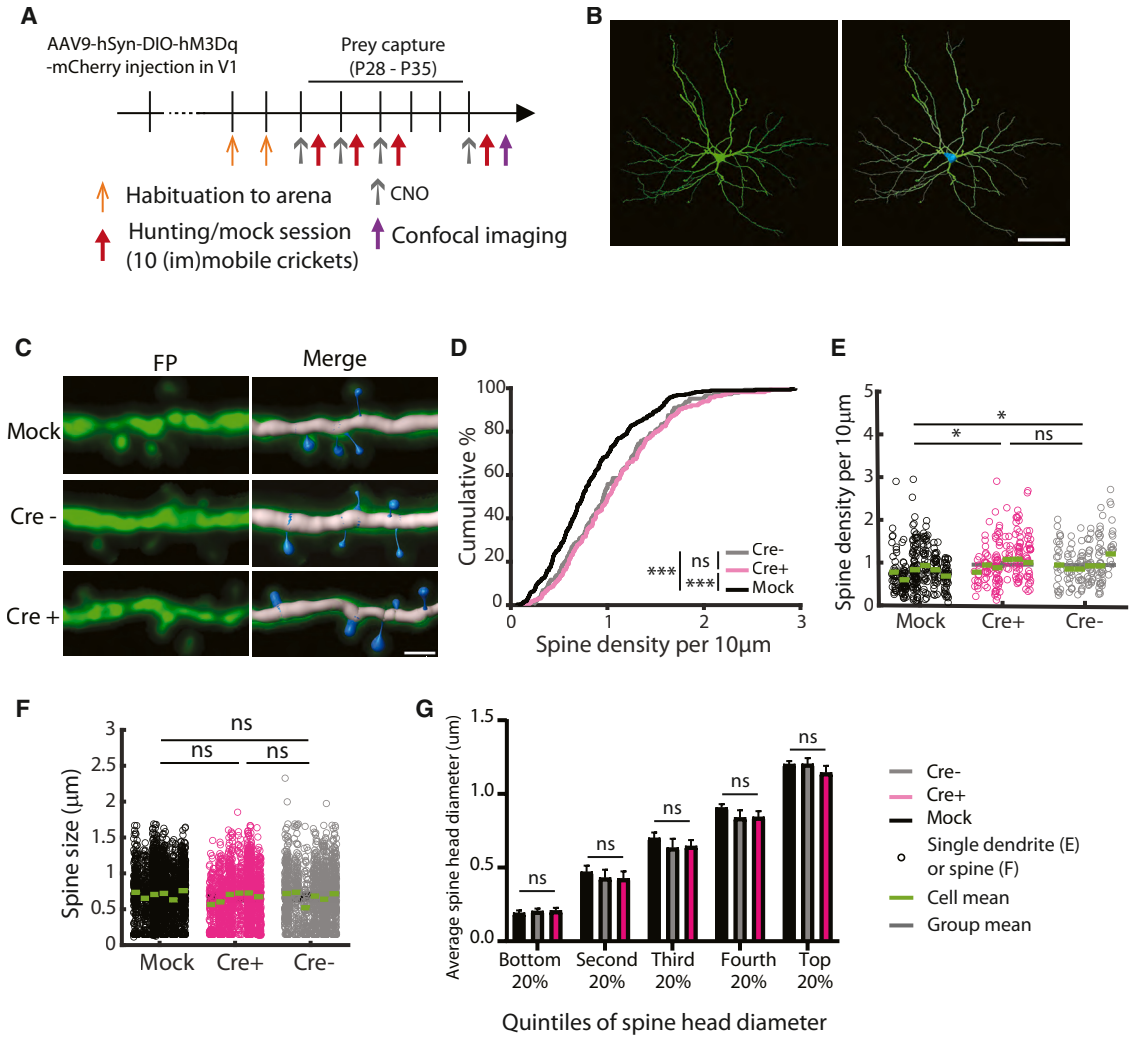

Figure 5. Prey capture learning induces a V1-independent increase in spine density in widefield cells (WF) of the superficial SC

(A) Experimental timeline with V1 inactivation and perfusion.

(B) Representative WF image (left), merged with its Imaris reconstruction (right). Scale bar, 200µm.

(C) Representative images of WF dendrites (left), merged with their Imaris reconstructions (right), from mock (top), hunting PV-Cre^{-} (middle), and PV-Cre^{+} (bottom) mice. Scale bar, 5 µm.

(D and E) Cumulative distribution across all animals (D) and nested analysis (E) of WF spine density. n = 288 dendrites (mock), 145 dendrites (hunting PV-Cre^{-}), and 165 dendrites (hunting PV-Cre^{+}). (D–G) Data from 6 neurons from 3–4 mice per condition.

(F) Nested analysis of WF spine size. n = 2,367 spines (mock), 1,492 spines (hunting PV-Cre^{-}), and 1,573 spines (hunting PV-Cre^{+}).

(G) Average spine head diameter per quintile from mock, hunting PV-Cre^{-}, and hunting PV-Cre^{+} mice. Spines were divided into equally sized quintiles for each neuron, and the average per condition calculated from all neurons from that condition. Mean ± SEM.

*p < 0.05 and ***p < 0.001.

See Figure S5 and Table S1.

synapse elimination, or both. To measure these dynamics, we implanted cranial windows over V1b in juvenile Thy1-YFP mice and ran them through our learning paradigm, while imaging the same L5 apical dendrites daily using *in vivo* two-photon imaging in awake, head-fixed mice (Figures 7A and 7B). The first imaging session took place after the second habituation session and served as baseline (day 0). In a subset of mice, we performed intrinsic signal imaging to confirm the placement of the cranial window over V1b (Figures S7A and S7B).

Mock mice showed a remarkably constant spine density throughout the experiment (Figure 7C), with little variation in the well-matched rates of spine formation and loss (Figures 7D and 7E). In marked contrast, spine density dramatically increased in hunting mice after the first hunting session, then reached a new higher plateau that persisted until the end of the experiment (Figure 7C). This was mediated by an immediate spike in spine formation, which decreased after day 1 but remained higher than in mock mice (Figure 7D), and a more gradual

Please cite this article in press as: Bissen et al., Ethological learning during the critical period resets synaptic setpoints in mouse binocular visual cortex, Neuron (2026), https://doi.org/10.1016/j.neuron.2026.06.016

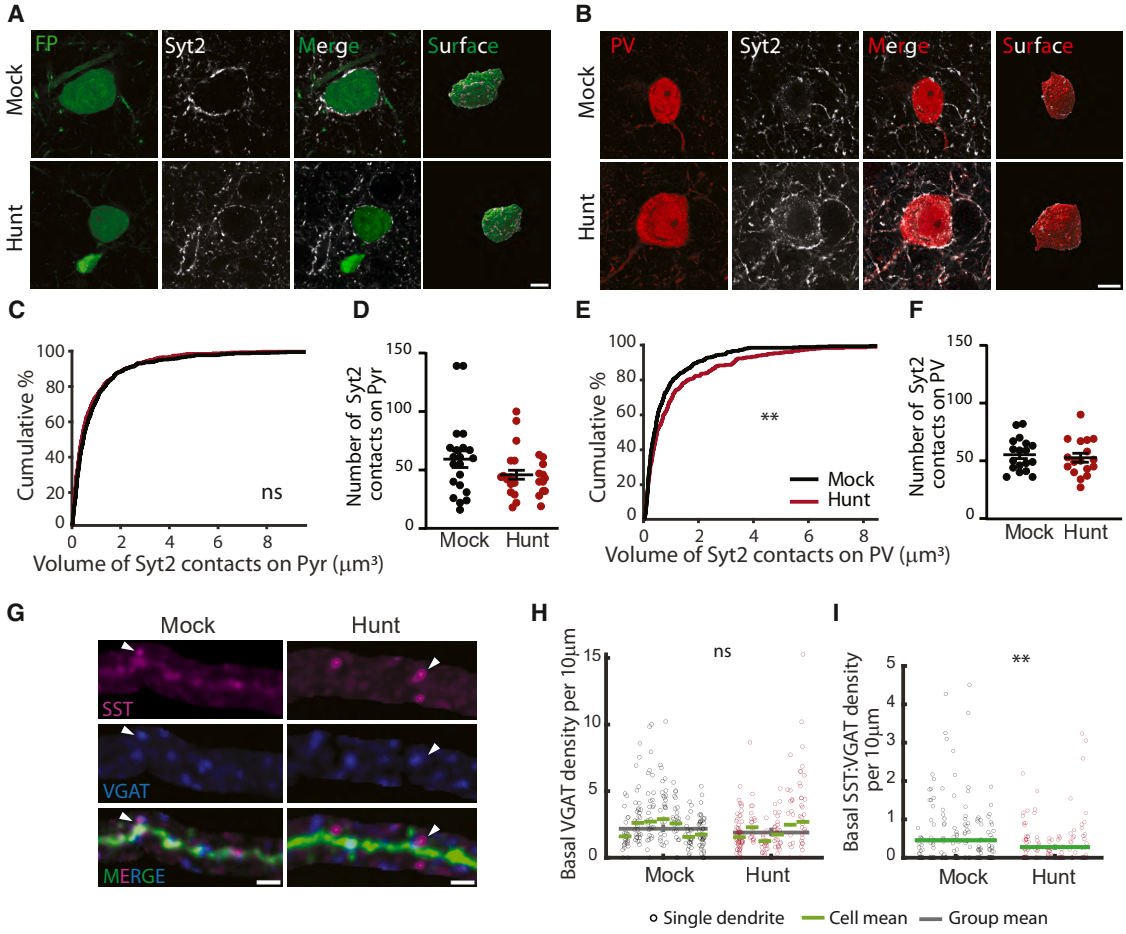

Figure 6. Global inhibition onto L5 pyramidal neurons is unchanged in hunting mice

(A and B) Representative images of an L5 pyramidal soma labeled for GFP (green, A) or an L5 PV soma labeled for PV (red, B) and Syt2 (white), with the merged image (right) and reconstructed surface (most right). Top or bottom row from a mock or hunting mouse, respectively. Scale bar, 10 μm.

(C and D) Cumulative distribution of the volume (C) and mean number (± SEM, D) of all Syt2$^+$ > YFP$^+$ L5 pyramidal somata contacts. *n* = 574 surfaces from 24 neurons (mock) and 649 surfaces from 27 neurons (hunting) from 3 mice per condition.

(E and F) Same as (C) and (D), but upon L5 PV$^+$ somata. *n* = 534 surfaces from 18 neurons (mock) and 300 surfaces from 17 neurons (hunting) from 3 mice per condition.

(G) Representative images of dendrites labeled for SST (magenta) and VGAT (blue), with the merged image with FP (green). Scale bar, 2 μm.

(H and I) Nested analysis of VGAT puncta (H) or SST:VGAT puncta (I) density along L5 pyramidal basal dendrites. *n* = 205 dendrites (mock) and 170 dendrites (hunting) from 6 neurons from 3 animals per condition.

*$p < 0.05$ and **$p < 0.01$.

See Figure S6 and Table S1.

increase in spine loss (Figure 7E). As a consequence of this offset in timing, net spine addition peaked on day 1 before slowly returning to 0 (Figure 7F), consistent with the density plateau (Figure 7C). However, as spine formation and elimination remain higher in hunting mice, these results indicate that L5 synapses remain in a highly plastic state days after learning, even though spine density stabilized. Intriguingly, we found little to no change in spine density (Figure 7C) or dynamics (Figures S7C–S7E) in extrastriate visual areas of hunting mice, indicating that these changes are specific to V1b.

Remarkably, the magnitude of the spine density increase on day 1 was predictive of improved performance on day 6 (Figure 7G). Further, the degree of learning on day 1 (calculated as the ratio of time to capture during the second and first half of the session) was predictive of greater spine formation on that day (Figure 7H). Prey capture learning thus shifts L5 pyramidal neurons, specifically in V1b, into a more connected and dynamic state in a manner that is directly correlated with behavioral improvement.

Blocking TNF-α-dependent signaling impairs prey capture learning and its underlying structural and functional plasticity

Prey capture learning in CP mice increases synapse density in V1b to a new, higher, and stable plateau, while also increasing spine dynamics (Figure 7). This stability in the midst of high

Please cite this article in press as: Bissen et al., Ethological learning during the critical period resets synaptic setpoints in mouse binocular visual cortex, Neuron (2026), https://doi.org/10.1016/j.neuron.2026.06.016

CellPress
OPEN ACCESS

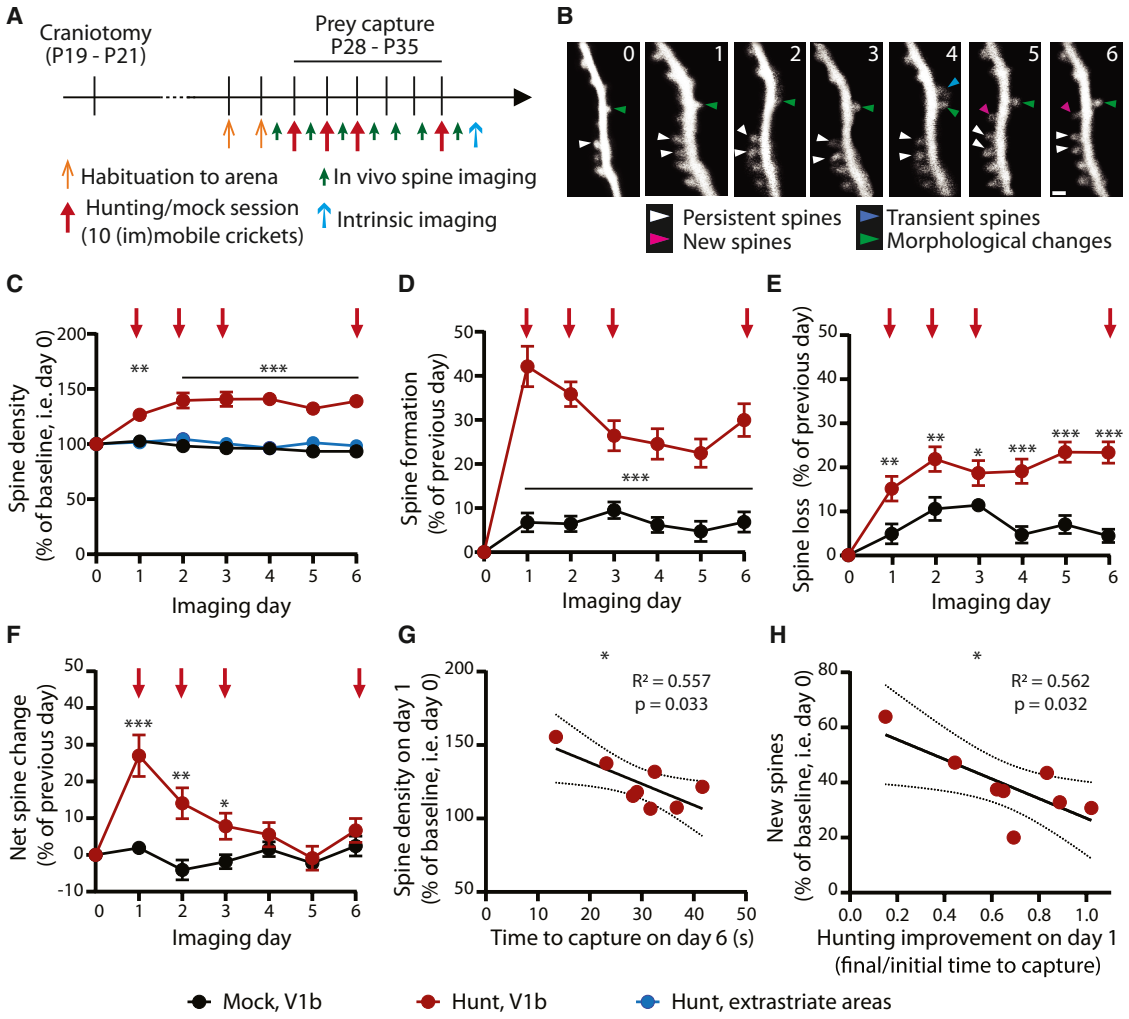

Figure 7. Hunting persistently enhances spine turnover of L5 pyramidal neurons

(A) Experimental timeline with chronic *in vivo* spine imaging in awake CP mice.

(B) Representative images of the same dendrite imaged daily. Scale bar, 2μm.

(C) Average spine density as a percentage of baseline (day 0). The density of each dendrite was normalized to its own baseline, and then the average was calculated across all dendrites for that condition. Mean ± SEM.

(D and E) Average spine formation (D) and loss (E) as a percentage of the previous day. Spine formation or loss on each dendrite was normalized to its corresponding value for the previous day, and then the average was calculated across all dendrites of that condition. Mean ± SEM.

(F) Average net spine change, calculated as the difference between spine formation and loss as a percentage of the previous day (i.e., F = D – E). Mean ± SEM.

(C–F) $n = 12$ dendrites from 4 mice (V1b, mock), 19 dendrites from 8 mice (hunting, V1b), and 12 dendrites from 4 mice (hunting, extrastriate). Asterisks represent statistical comparisons between hunting and mock at each session.

(G) Spine density on day 1 (calculated as in C) as a function of the time to cricket capture (TTC) on day 6 (s).

(H) Spine formation on day 1 (calculated as in D) as a function of the hunting improvement on day 1 (calculated as average TTC for the second half [final] divided by average TTC for the first half [initial] on day 1).

(G and H) Red dots represent individual hunting animals ($N = 8$), the black line a simple linear regression fit, and the dotted lines the borders of the 95% confidence interval.

*$p < 0.05$, **$p < 0.01$, and ***$p < 0.001$.

See Figure S7 and Table S1.

plasticity suggests that there are mechanisms in place to move spine density to, and then constrain it at, this new value. Additionally, spine density increases are widespread, suggesting this process is not mediated by a synapse-specific mechanism (Figure 3). One global synaptic plasticity mechanism known to mediate increases in both synapse number and strength *in vitro*[77–81] and in V1 after sensory deprivation[24,55,81,82] is excitatory synaptic scaling.

To test the possible involvement of homeostatic synaptic plasticity, we treated animals with XPro1595, an inhibitor of tumor necrosis factor (TNF)-α signaling that blocks upscaling but not downscaling or Hebbian plasticity.[55,56,83,84] We ran CP

Please cite this article in press as: Bissen et al., Ethological learning during the critical period resets synaptic setpoints in mouse binocular visual cortex, Neuron (2026), https://doi.org/10.1016/j.neuron.2026.06.016

Thy1-YFP mice through our paradigm and treated them with XPro 1 h after the first hunting or mock session and again on day 3 to continuously block TNF-α-dependent pathways after the initial acquisition of hunting skills (Figure 8A). We then quantified spine density and morphology on day 6 (Figure 8B). In stark contrast to our previous findings (Figures 3F, 3G, and S3B–S3E), neither L5 (Figures 8C, 8D, and S8A–S8C) nor L2/3 pyramidal (Figures S8D and S8E) spine density increased in XPro-treated hunting mice, with a significant interaction between drug treatment and behavior (hunting vs. mock) and a significant increase in spine density in the control but not XPro condition (Figure 8E). The long-term structural plasticity driven by prey capture learning in V1b is thus TNF-α-dependent.

Since XPro administration was systemic, it could also affect plasticity in the SC. To determine whether the learning-induced increase in spine density in WF cells (Figures 5 and S5) also depended on TNF-α signaling, we quantified spine changes in WF cells in the same XPro-treated mice and found that this increase was blocked (Figures S8F–S8H). TNF-α signaling, hence, plays a critical role in enabling long-term learning-related structural plasticity across cortical and subcortical visual areas.

As prey capture learning enhances TF discrimination (Figure 2), we next asked whether this refinement of visual function also depends on TNF-α signaling. We assessed TF tuning in L2/3 neurons as before (Figure 2) from XPro-treated hunting and mock mice. Remarkably, XPro treatment prevented the drop in TF low-pass index normally induced by hunting (Figures 8F–8H). Thus, both structural remodeling and the enhancement in TF discrimination induced by prey capture learning are TNF-α-dependent.

Finally, if structural and functional plasticity are important for the learning and retention of hunting skills, then preventing them with XPro should also impair performance. To test this, we quantified prey capture learning for XPro-injected hunting and mock mice. While XPro-injected mice showed some improvement between day 1 and 2, performance plateaued at a significantly worse level than for their control counterparts (Figures 8I, S8I, and S8J), and attack duration did not decrease (Figures 8J–8L). This was not due to an initial deficit in learning, as XPro-injected and control mice improved similarly across the first hunting session prior to XPro injection (Figure S8K). Finally, XPro-injected and control mock mice showed no difference in their time to find immobilized crickets, indicating that inhibition of TNF-α signaling does not significantly impair basic visual and motor skills or appetitive drive (Figure S8N). Taken together, these results strongly suggest that the structural and functional changes in visual areas induced by prey capture learning are mediated by TNF-α-dependent plasticity and contribute to enhanced hunting proficiency.

DISCUSSION

CPs are windows of heightened experience-dependent plasticity believed to tune sensory circuitry to improve function.[1–3] However, whether V1 CP plasticity can indeed improve visual function during natural behaviors has proven difficult to address using classic sensory deprivation or alteration paradigms. Here, we used prey capture learning to assess the impact of ethological visual learning on V1b plasticity and function. Strikingly, we found that CP learning engages TNF-α-dependent mechanisms to increase spine turnover and stabilize spine density around a higher, stable setpoint, improve V1b TF discrimination, and enhance behavioral performance. Importantly, both the morphological and functional plasticity we identify are strongly correlated with skill acquisition and retention, suggesting that they contribute to behavioral improvement. Together, these findings show that active visuomotor learning during the V1 CP persistently shifts V1b excitatory circuitry into a more connected and dynamic state and suggest that this resetting is an important mediator of improved function. Finally, the dependence of this resetting on TNF-α signaling, which is essential for the expression of excitatory homeostatic plasticity,[55,56] suggests that learning co-opts homeostatic mechanisms to stabilize neocortical synaptic setpoints around new higher values.

Prey capture in expert mice relies on binocular vision,[50,52,53] with well-established roles for the retina and SC.[53,54,69,70] By contrast, a role for V1 has not previously been established, and the locus of learning-induced plasticity was unknown. We found that V1 inactivation during learning prevented learning-induced changes in L5 pyramidal spine density and reduced behavioral improvement. Prey capture learning thus relies on V1 in CP mice, as we recently found for CP rats.[48] Furthermore, these findings suggest that improvement in hunting efficiency arises in part through V1b remodeling. Moreover, while there are complementary changes in spine density onto widefield (WF) cells in the superficial SC, which are known to contribute to prey detection and pursuit initiation,[53] this remodeling is unaffected by V1 inactivation, indicating that prey capture learning drives V1b and SC structural plasticity through parallel pathways. This dual engagement of subcortical and cortical visual pathways suggests that they may mediate distinct but complementary aspects of the visual processing underlying prey capture learning. While mice can perform simple visually guided operant behaviors during V1 silencing, likely via subcortical pathways, recent literature suggests that V1 is indispensable for complex visual discrimination tasks.[85–90] A similar duality between instinctive, immediate responses and flexible adaptations to environmental variations, which do not always rely on direct corticocollicular projections,[91] has been proposed for threat responses[92] and is likely during other complex natural behaviors such as prey capture learning. Our data thus fit within a larger framework suggesting that plasticity within visual cortical and subcortical pathways work in concert to enable fine-tuned, visually guided, natural adaptive behaviors.

Predation is a complex behavior modulated by other elements besides visuomotor learning, such as arousal and appetitive drive,[59,93,94] which could influence predation-induced changes in V1b. We thus compared hunting mice to control animals that received immobilized crickets in mock "hunting" sessions akin to foraging and therefore experienced similar novelty exposure and food deprivation-induced motivation. Careful behavioral analysis indicates that hunting and mock mice display similar levels of exploration and motivation to find and consume crickets. Strikingly, mock mice show stable spine density and dynamics, in contrast to the synaptic pruning normally shown during late development in V1,[31,95] suggesting that the mock

Please cite this article in press as: Bissen et al., Ethological learning during the critical period resets synaptic setpoints in mouse binocular visual cortex, Neuron (2026), https://doi.org/10.1016/j.neuron.2026.06.016

CellPress
OPEN ACCESS

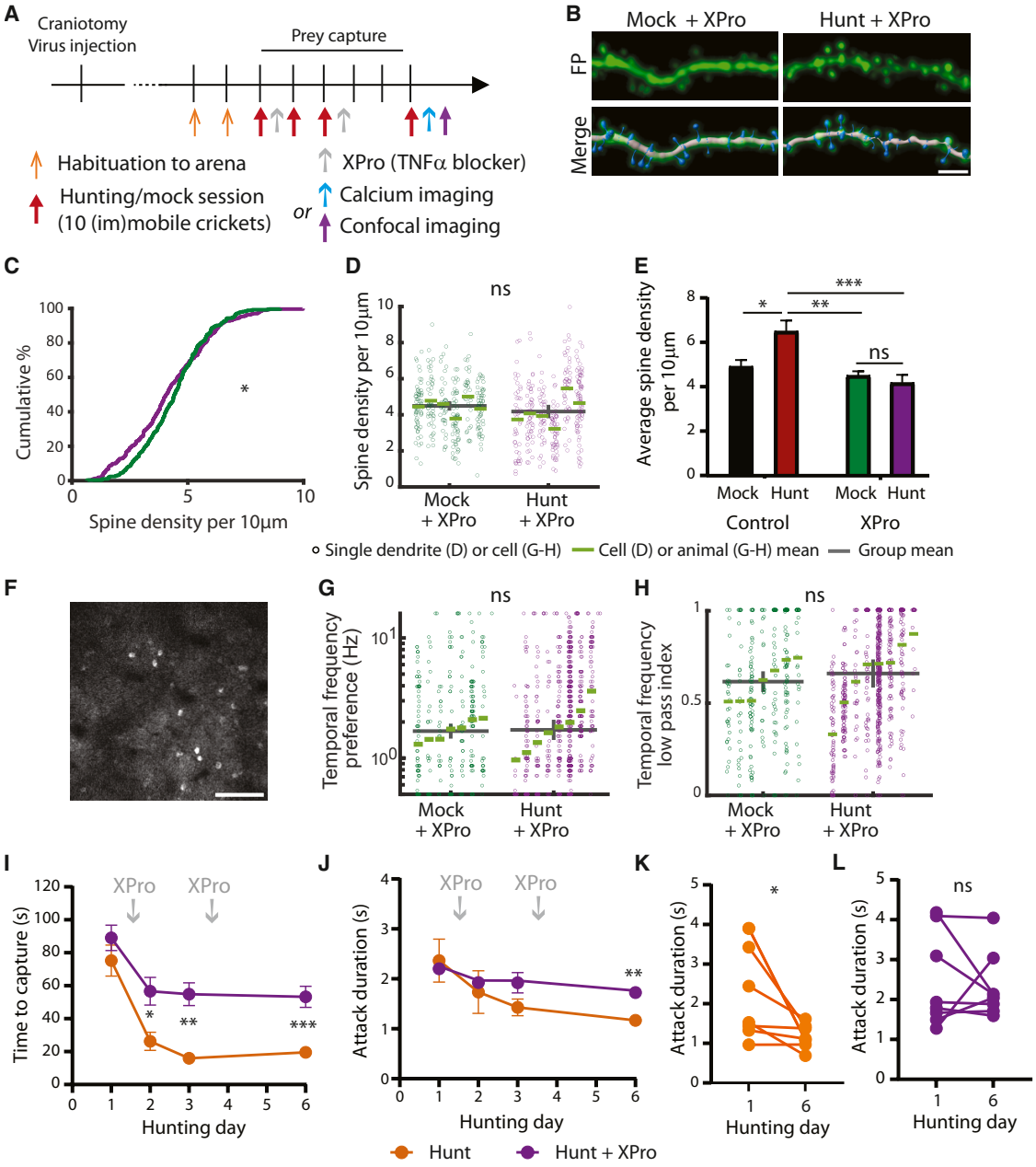

Figure 8. Blocking TNF-α-dependent signaling impairs structural and functional plasticity and prey capture learning

(A) Experimental timeline with XPro injections, followed by perfusion or calcium imaging.

(B) Representative images of dendrites (top) merged with their Imaris reconstructions (bottom) from mock + XPro (left) and hunting + XPro (right) mice. Scale bar, 5 µm.

(C and D) Cumulative distribution across all animals (C) or nested analysis (D) of spine density across all animals. *Nn*= 306 dendrites (mock + XPro) and 285 dendrites (hunting + XPro) from 6 neurons from 3 mice per condition.

(E) Average spine density for control and XPro-treated mice, from the cumulative distribution shown in Figure 3D (control) and in Figure 7C. *n*= 6 neurons from 3–4 mice per condition. Mean ± SEM.

(F) Representative two-photon image of GCaMP6s$^+$ L2/3 neurons from an XPro-treated mouse. Scale bar, 100 µm.

(G and H) TF preference (Hz, G) and LPI (Hz, H) for XPro-treated mock and hunting mice. *n* = 1,145 cells from 7 mice (mock) and 832 from 8 mice (hunting).

(I and J) Average time to capture (TTC, s, I) or attack duration (s, J) for each hunting session (10 crickets) across all animals. *N* = 8 hunting + XPro mice and 8 hunting mice. Mean ± SEM.

(K and L) Average attack duration (s) for each non-injected (K) or XPro-injected (L) mouse on day 1 and day 6.

*$p < 0.05$, **$p < 0.01$, and ***$p < 0.001$.

See Figure S8 and Table S1.

Please cite this article in press as: Bissen et al., Ethological learning during the critical period resets synaptic setpoints in mouse binocular visual cortex, Neuron (2026), https://doi.org/10.1016/j.neuron.2026.06.016

paradigm is sufficient to reduce synapse elimination. This effect is reminiscent of the effects of EEs, which can delay spine pruning in juvenile V1[95] and increase spine formation and density in adult V1.[96] Intriguingly, EE also accelerates visual function development through enhanced maternal care and earlier eye opening[97] but does not ultimately improve adult visual function.[98] While multiple mechanisms have been suggested to mediate EE effects, no unifying framework has emerged, likely due to large experimental paradigm variability.[99] Here, we compared carefully matched mock and hunt paradigms to allow us to differentiate between effects arising from general enrichment (foraging for novel treats) and those driven by active pursuit of prey. The enhanced structural plasticity and TF discrimination we observed in hunting mice is, therefore, driven not through non-specific EE but instead by active visuomotor learning.

Interestingly, while prey capture learning had little effect on most RF properties, it improved TF discrimination by increasing the proportion of V1b neurons narrowly tuned for specific TFs. This suggests that hunting mice are better at discriminating objects moving at different speeds and is consistent with the demonstration that experienced hunters preferentially approach visual stimuli matching cricket size and speed.[52,100] As TF discrimination is well-correlated with hunting efficacy, our data suggest that learning-induced TF changes contribute to behavioral improvement. The precise mechanisms of TF tuning in V1 remain unknown,[101–103] and in young cats[6] and ferrets[104,105] TF tuning is unaffected by dark rearing or exposure to artificially altered visual stimuli. TF tuning is, however, degraded by premature visual experience in ferrets, leading to impaired motion processing—the converse effect we find here for prey capture learning.[106] Taken with previous work, our data thus indicate that while TF tuning during development is largely robust to artificially altering or withdrawing visual experience, it can be rapidly and persistently improved by chasing moving prey. This finding highlights the importance of using ethological paradigms to assess the role of CP plasticity in modulating behaviorally relevant features of visual processing.

Prey capture learning induced widespread structural plasticity across cortical layers in V1b. Hunting mice showed a dramatic and persistent increase in L5 pyramidal spine density and dynamics due to an immediate increase in spine formation followed by a slower increase in spine loss. At first glance, this time course is the reciprocal of changes observed during monocular deprivation in CP V1b: decreased spine density due to higher spine elimination, with a delayed elevation in spine formation[16,17,20] and motility.[18,19] However, these deprivation-induced changes are transient, with spine dynamics returning to control levels shortly after eye reopening.[17] They also contrast with the transient enhancement of ocular dominance plasticity in V1[107] and spine turnover in motor cortex during EE,[44] which reverses upon return to standard housing. By contrast, after prey capture learning, spine turnover remains at a stable elevated plateau for at least 3 days after the cessation of hunting, suggesting that this brief (30 hunts of about 1 min across 3 days) but salient experience drives a persistent elevation in spine density and dynamics. These effects are reminiscent of the effects of learning in the motor cortex of adolescent mice, which can also induce a long-lasting increase in spine dynamics enduring beyond motor training.[44,108] Thus, our data suggest that learning can induce similar structural plasticity in the motor and sensory neocortex of young animals.

Prey capture learning-induced synaptic remodeling onto L5 pyramidal neurons selectively targets excitatory circuitry, as we observed no significant changes in perisomatic or dendritic inhibitory contacts. This is consistent with our recent observation that prey capture learning persistently increases firing rates in putative pyramidal neurons in V1b in CP rats.[48] Our data thus suggest that prey capture learning rewires V1b circuitry to increase net excitatory drive onto L5 pyramidal neurons. This widespread resetting of synaptic density, coupled with enhanced spine dynamics, is likely important for enabling the selective incorporation of new behaviorally relevant connections during learning and consolidation, without compromising existing circuitry.

In stark contrast to CP mice, adult hunters showed no persistent structural plasticity in V1b, despite learning the task at a similar rate. In adult V1, repetitive exposure to the same visual stimulus has produced conflicting results on spine density.[67,68] However, while learning can transiently modulate spine density in the adult cortex,[109–112] a large body of work finds little to no long-term effect on spine density,[36–39] consistent with the remarkable overall stability of adult cortical circuitry[31–35] and activity.[24–30] In all cases, learning remodels a small fraction of dendritic spines by enhancing turnover, precisely rewiring behaviorally relevant circuitry while keeping the broader network intact.[22,23,41,113] While adults may show transient changes in density that then reverse, our data make clear that in adult V1b, prey capture learning does not trigger the same persistent increase in spine density seen during the CP. This is consistent with a substantial literature showing that the effects of sensory deprivation on adult V1 are markedly different than CP V1, with fewer structural changes,[55,114–116] unaffected RF properties,[14,15,117] and the potentiation phase of ocular dominance (OD) plasticity mediated by different (αCaMKII-dependent vs. TNF-α-dependent) mechanisms.[12,82,118–121] Our results thus fit with a model in which TNF-α-dependent homeostatic mechanisms are selectively engaged to remodel circuitry during the visual CP.

Taken together, our data suggest that ethological learning is uniquely capable of adjusting V1 excitatory synaptic setpoints during the CP. Prey capture learning moves spine density to a new, elevated steady-state with enhanced dynamics. Spine density is thus malleable and can be reset by learning, where it is then stabilized by mechanisms that tightly match synapse formation and loss. This remodeling is widespread across apical and basal dendrites rather than targeted to a small subset of spines and likely cooperates with increased synaptic turnover to bias the presynaptic source of these inputs to enhance the ability of V1b to detect and track prey during active sensing, in collaboration with subcortical visual circuitry remodeling. Because this synaptic resetting is slow, widespread, and TNF-α-dependent, it is likely driven by homeostatic rather than Hebbian mechanisms, yet it diverges from the traditional view of homeostasis as a return to baseline. While Hebbian plasticity is widely appreciated to contribute to learning (reviewed in Dringenberg et al.[122]), the role of homeostatic plasticity in learning

and memory consolidation remains underexplored and to date has been confined to a role in downscaling synaptic strength to promote memory extinction[123] or specificity.[124] Here, we find that ethological CP learning co-opts upward homeostatic plasticity to move synaptic weight bounds to new, higher values, a process important for memory retention. Confining this resetting to the CP may ensure that ethologically relevant visual behavior can match visual cortical networks to likely environmental demands without rendering them vulnerable to the effects of aberrant experiences throughout life. Finally, our data suggest that enhanced visual experience during the CP drives visual circuitry into a more dynamic state, which could support future experience-dependent plasticity to facilitate the successful integration of subsequent learning events.

RESOURCE AVAILABILITY

Lead contact

Further information and requests for reagents and resources should be directed to and will be fulfilled by the lead contact, Gina Turrigiano (turrigiano@brandeis.edu).

Materials availability

This study did not generate any new reagents.

Data and code availability

The imaging data supporting this study have not been deposited in a public repository because there is currently no standardized format or repository for such data but are available from the corresponding author upon request (turrigiano@brandeis.edu). All code has been deposited on GitHub (see STAR Methods). Any additional information required to reanalyze the data from this study is available from the lead contact upon request.

ACKNOWLEDGMENTS

We thank Christine Grienberger for assistance with cranial window implantation, Benjamin Scholl with the subcellular registration of *in vivo* images, Mark Andermann for help confirming cranial window localization, and the Brandeis Light Microscopy Core Facility. Schematics created with SciDraw.com. This work was supported by NIH grants R01 EY025613 and R35 NS111562 (G.G.T.).

AUTHOR CONTRIBUTIONS

Conceptualization, D.B., S.D.V.H., and G.G.T.; methodology, D.B., S.D.V.H., and G.G.T.; software, B.A.C. and K.A.S.; investigation, D.B. and W.W.; formal analysis, D.B., B.A.C., A.Z., and W.W.; writing – original draft, D.B. and G.G.T.; writing – review & editing, D.B., S.V.D.H., and G.G.T.; funding acquisition, G.G.T.; resources, S.D.V.H. and G.G.T.; and supervision, G.G.T.

DECLARATION OF INTERESTS

The authors declare no competing interests.

STAR★METHODS

Detailed methods are provided in the online version of this paper and include the following:

- KEY RESOURCES TABLE
- EXPERIMENTAL MODEL AND STUDY PARTICIPANT DETAILS
  - Animals
- METHOD DETAILS
  - Prey capture learning paradigm
  - Cranial window surgery and GCaMP6s virus injection
  - XPro51595 administration
  - Chemogenetic experiments and CNO injection
  - *In vivo* imaging
  - *Ex vivo* slice electrophysiology
  - Immunostaining and confocal microscopy
- QUANTIFICATION AND STATISTICAL ANALYSIS
  - Behavioral analysis
  - Chronic spine imaging analysis
  - Confocal image acquisition and analysis
  - Intrinsic imaging analysis
  - Calcium imaging analysis
  - mEPSC recordings
  - Statistical analysis

SUPPLEMENTAL INFORMATION

Supplemental information can be found online at https://doi.org/10.1016/j.neuron.2026.06.016.

Received: February 3, 2025
Revised: April 13, 2026
Accepted: June 17, 2026

REFERENCES

1. Hooks, B.M., and Chen, C. (2020). Circuitry Underlying Experience-Dependent Plasticity in the Mouse Visual System. Neuron *106*, 21–36. https://doi.org/10.1016/j.neuron.2020.01.031.
2. Reh, R.K., Dias, B.G., Nelson, C.A., Kaufer, D., Werker, J.F., Kolb, B., Levine, J.D., and Hensch, T.K. (2020). Critical period regulation across multiple timescales. Proc. Natl. Acad. Sci. USA *117*, 23242–23251. https://doi.org/10.1073/pnas.1820836117.
3. Hensch, T.K. (2005). Critical Period Mechanisms in Developing Visual Cortex. In Curr. Top. Dev. Biol., *69* (Elsevier), pp. 215–237. https://doi.org/10.1016/S0070-2153(05)69008-4.
4. Kreile, A.K., Bonhoeffer, T., and Hübener, M. (2011). Altered Visual Experience Induces Instructive Changes of Orientation Preference in Mouse Visual Cortex. J. Neurosci. *31*, 13911–13920. https://doi.org/10.1523/JNEUROSCI.2143-11.2011.
5. Li, Y., Van Hooser, S.D., Mazurek, M., White, L.E., and Fitzpatrick, D. (2008). Experience with moving visual stimuli drives the early development of cortical direction selectivity. Nature *456*, 952–956. https://doi.org/10.1038/nature07417.
6. Humphrey, A.L., and Saul, A.B. (1998). Strobe Rearing Reduces Direction Selectivity in Area 17 by Altering Spatiotemporal Receptive-Field Structure. J. Neurophysiol. *80*, 2991–3004. https://doi.org/10.1152/jn.1998.80.6.2991.
7. Blakemore, C., and Mitchell, D.E. (1973). Environmental Modification of the Visual Cortex and the Neural Basis of Learning and Memory. Nature *241*, 467–468. https://doi.org/10.1038/241467a0.
8. Roy, A., Wang, S., Meschede-Krasa, B., Breffle, J., and Van Hooser, S.D. (2020). An early phase of instructive plasticity before the typical onset of sensory experience. Nat. Commun. *11*, 11. https://doi.org/10.1038/s41467-019-13872-1.
9. Brown, T.C., and McGee, A.W. (2023). Monocular deprivation during the critical period alters neuronal tuning and the composition of visual circuitry. PLOS Biol. *21*, e3002096. https://doi.org/10.1371/journal.pbio.3002096.
10. Smith, S.L., and Trachtenberg, J.T. (2007). Experience-dependent binocular competition in the visual cortex begins at eye opening. Nat. Neurosci. *10*, 370–375. https://doi.org/10.1038/nn1844.
11. Wiesel, T.N., and Hubel, D.H. (1963). SINGLE-CELL RESPONSES IN STRIATE CORTEX OF KITTENS DEPRIVED OF VISION IN ONE EYE.

J. Neurophysiol. *26*, 1003–1017. https://doi.org/10.1152/jn.1963.26.6.1003.

12. Frenkel, M.Y., and Bear, M.F. (2004). How Monocular Deprivation Shifts Ocular Dominance in Visual Cortex of Young Mice. Neuron *44*, 917–923. https://doi.org/10.1016/j.neuron.2004.12.003.
13. Gordon, J.A., and Stryker, M.P. (1996). Experience-Dependent Plasticity of Binocular Responses in the Primary Visual Cortex of the Mouse. J. Neurosci. *16*, 3274–3286. https://doi.org/10.1523/JNEUROSCI.16-10-03274.1996.
14. Levine, J.N., Chen, H., Gu, Y., and Cang, J. (2017). Environmental Enrichment Rescues Binocular Matching of Orientation Preference in the Mouse Visual Cortex. J. Neurosci. *37*, 5822–5833. https://doi.org/10.1523/JNEUROSCI.3534-16.2017.
15. Wang, B.-S., Sarnaik, R., and Cang, J. (2010). Critical Period Plasticity Matches Binocular Orientation Preference in the Visual Cortex. Neuron *65*, 246–256. https://doi.org/10.1016/j.neuron.2010.01.002.
16. Zhou, Y., Lai, B., and Gan, W.-B. (2017). Monocular deprivation induces dendritic spine elimination in the developing mouse visual cortex. Sci. Rep. *7*, 4977. https://doi.org/10.1038/s41598-017-05337-6.
17. Sun, Y.J., Espinosa, J.S., Hoseini, M.S., and Stryker, M.P. (2019). Experience-dependent structural plasticity at pre- and postsynaptic sites of layer 2/3 cells in developing visual cortex. Proc. Natl. Acad. Sci. USA *116*, 21812–21820. https://doi.org/10.1073/pnas.1914661116.
18. Majewska, A., and Sur, M. (2003). Motility of dendritic spines in visual cortex *in vivo*: Changes during the critical period and effects of visual deprivation. Proc. Natl. Acad. Sci. USA *100*, 16024–16029. https://doi.org/10.1073/pnas.2636949100.
19. Oray, S., Majewska, A., and Sur, M. (2004). Dendritic Spine Dynamics Are Regulated by Monocular Deprivation and Extracellular Matrix Degradation. Neuron *44*, 1021–1030. https://doi.org/10.1016/j.neuron.2004.12.001.
20. Mataga, N., Mizuguchi, Y., and Hensch, T.K. (2004). Experience-Dependent Pruning of Dendritic Spines in Visual Cortex by Tissue Plasminogen Activator. Neuron *44*, 1031–1041. https://doi.org/10.1016/j.neuron.2004.11.028.
21. Wallace, W., and Bear, M.F. (2004). A Morphological Correlate of Synaptic Scaling in Visual Cortex. J. Neurosci. *24*, 6928–6938. https://doi.org/10.1523/JNEUROSCI.1110-04.2004.
22. Runge, K., Cardoso, C., and De Chevigny, A. (2020). Dendritic Spine Plasticity: Function and Mechanisms. Front. Synaptic Neurosci. *12*, 36. https://doi.org/10.3389/fnsyn.2020.00036.
23. Guo, H., Ali, T., Que, J., Zhou, Y., and Bai, Y. (2023). Dendritic spine dynamics in associative memory: A comprehensive review. FASEB J. *37*, e22896. https://doi.org/10.1096/fj.202202166R.
24. Hengen, K.B., Lambo, M.E., Van Hooser, S.D., Katz, D.B., and Turrigiano, G.G. (2013). Firing Rate Homeostasis in Visual Cortex of Freely Behaving Rodents. Neuron *80*, 335–342. https://doi.org/10.1016/j.neuron.2013.08.038.
25. Hengen, K.B., Torrado Pacheco, A., McGregor, J.N., Van Hooser, S.D., and Turrigiano, G.G. (2016). Neuronal Firing Rate Homeostasis Is Inhibited by Sleep and Promoted by Wake. Cell *165*, 180–191. https://doi.org/10.1016/j.cell.2016.01.046.
26. Torrado Pacheco, A., Bottorff, J., Gao, Y., and Turrigiano, G.G. (2021). Sleep Promotes Downward Firing Rate Homeostasis. Neuron *109*, 530–544.e6. https://doi.org/10.1016/j.neuron.2020.11.001.
27. Wu, Y.K., Hengen, K.B., Turrigiano, G.G., and Gjorgjieva, J. (2020). Homeostatic mechanisms regulate distinct aspects of cortical circuit dynamics. Proc. Natl. Acad. Sci. USA *117*, 24514–24525. https://doi.org/10.1073/pnas.1918368117.
28. Dhawale, A.K., Poddar, R., Wolff, S.B., Normand, V.A., Kopelowitz, E., and Ölveczky, B.P. (2017). Automated long-term recording and analysis of neural activity in behaving animals. eLife *6*, e27702. https://doi.org/10.7554/eLife.27702.
29. McGregor, J.N., Farris, C.A., Ensley, S., Schneider, A., Fosque, L.J., Wang, C., Tilden, E.I., Liu, Y., Tu, J., Elmore, H., et al. (2024). Failure in a population: Tauopathy disrupts homeostatic set-points in emergent dynamics despite stability in the constituent neurons. Neuron *112*, 3567–3584.e5. https://doi.org/10.1016/j.neuron.2024.08.006.
30. Jensen, K.T., Kadmon Harpaz, N., Dhawale, A.K., Wolff, S.B.E., and Ölveczky, B.P. (2022). Long-term stability of single neuron activity in the motor system. Nat. Neurosci. *25*, 1664–1674. https://doi.org/10.1038/s41593-022-01194-3.
31. Grutzendler, J., Kasthuri, N., and Gan, W.-B. (2002). Long-term dendritic spine stability in the adult cortex. Nature *420*, 812–816. https://doi.org/10.1038/nature01276.
32. Zuo, Y., Lin, A., Chang, P., and Gan, W.-B. (2005). Development of Long-Term Dendritic Spine Stability in Diverse Regions of Cerebral Cortex. Neuron *46*, 181–189. https://doi.org/10.1016/j.neuron.2005.04.001.
33. Holtmaat, A.J.G.D., Trachtenberg, J.T., Wilbrecht, L., Shepherd, G.M., Zhang, X., Knott, G.W., and Svoboda, K. (2005). Transient and Persistent Dendritic Spines in the Neocortex In Vivo. Neuron *45*, 279–291. https://doi.org/10.1016/j.neuron.2005.01.003.
34. Trachtenberg, J.T., Chen, B.E., Knott, G.W., Feng, G., Sanes, J.R., Welker, E., and Svoboda, K. (2002). Long-term in vivo imaging of experience-dependent synaptic plasticity in adult cortex. Nature *420*, 788–794. https://doi.org/10.1038/nature01273.
35. Majewska, A.K., Newton, J.R., and Sur, M. (2006). Remodeling of Synaptic Structure in Sensory Cortical Areas In Vivo. J. Neurosci. *26*, 3021–3029. https://doi.org/10.1523/JNEUROSCI.4454-05.2006.
36. Albarran, E., Raissi, A., Jáidar, O., Shatz, C.J., and Ding, J.B. (2021). Enhancing motor learning by increasing the stability of newly formed dendritic spines in the motor cortex. Neuron *109*, 3298–3311.e4. https://doi.org/10.1016/j.neuron.2021.07.030.
37. Peters, A.J., Chen, S.X., and Komiyama, T. (2014). Emergence of reproducible spatiotemporal activity during motor learning. Nature *510*, 263–267. https://doi.org/10.1038/nature13235.
38. Chen, S.X., Kim, A.N., Peters, A.J., and Komiyama, T. (2015). Subtype-specific plasticity of inhibitory circuits in motor cortex during motor learning. Nat. Neurosci. *18*, 1109–1115. https://doi.org/10.1038/nn.4049.
39. Moczulska, K.E., Tinter-Thiede, J., Peter, M., Ushakova, L., Wernle, T., Bathellier, B., and Rumpel, S. (2013). Dynamics of dendritic spines in the mouse auditory cortex during memory formation and memory recall. Proc. Natl. Acad. Sci. USA *110*, 18315–18320. https://doi.org/10.1073/pnas.1312508110.
40. Harris, K.M. (2020). Structural LTP: from synaptogenesis to regulated synapse enlargement and clustering. Curr. Opin. Neurobiol. *63*, 189–197. https://doi.org/10.1016/j.conb.2020.04.009.
41. Fu, M., and Zuo, Y. (2011). Experience-dependent structural plasticity in the cortex. Trends Neurosci. *34*, 177–187. https://doi.org/10.1016/j.tins.2011.02.001.
42. Chambers, A.R., and Rumpel, S. (2017). A stable brain from unstable components: Emerging concepts and implications for neural computation. Neuroscience *357*, 172–184. https://doi.org/10.1016/j.neuroscience.2017.06.005.
43. Butz, M., Wörgötter, F., and Van Ooyen, A. (2009). Activity-dependent structural plasticity. Brain Res. Rev. *60*, 287–305. https://doi.org/10.1016/j.brainresrev.2008.12.023.
44. Yang, G., Pan, F., and Gan, W.-B. (2009). Stably maintained dendritic spines are associated with lifelong memories. Nature *462*, 920–924. https://doi.org/10.1038/nature08577.
45. Jung, C.K.E., and Herms, J. (2014). Structural Dynamics of Dendritic Spines are Influenced by an Environmental Enrichment: An In Vivo Imaging Study. Cereb. Cortex *24*, 377–384. https://doi.org/10.1093/cercor/bhs317.

46. Sale, A., Putignano, E., Cancedda, L., Landi, S., Cirulli, F., Berardi, N., and Maffei, L. (2004). Enriched environment and acceleration of visual system development. Neuropharmacology *47*, 649–660. https://doi.org/10.1016/j.neuropharm.2004.07.008.

47. Cancedda, L., Putignano, E., Sale, A., Viegi, A., Berardi, N., and Maffei, L. (2004). Acceleration of Visual System Development by Environmental Enrichment. J. Neurosci. *24*, 4840–4848. https://doi.org/10.1523/JNEUROSCI.0845-04.2004.

48. Leman, D.P., Cary, B.A., Bissen, D., Wen, W., Lane, B.J., Regis, M., Wong, N.F., Bhut, K.B., and Turrigiano, G.G. Rapid Prey Capture Learning Slowly Re-sets Activity Set Points in Rodent Binocular Visual Cortex Preprint at bioRxiv. https://doi.org/10.1101/2025.04.11.648036.

49. Groves Kuhnle, C., Grimes, M., Suárez Casanova, V.M., Turrigiano, G.G., and Van Hooser, S.D. (2022). Juvenile Shank3 KO Mice Adopt Distinct Hunting Strategies during Prey Capture Learning. eNeuro *9*. ENEURO.0230-22.2022. https://doi.org/10.1523/ENEURO.0230-22.2022.

50. Hoy, J.L., Yavorska, I., Wehr, M., and Niell, C.M. (2016). Vision Drives Accurate Approach Behavior during Prey Capture in Laboratory Mice. Curr. Biol. *26*, 3046–3052. https://doi.org/10.1016/j.cub.2016.09.009.

51. Berry, R.J., and Bronson, F.H. (1992). Life History AND BIOECONOMY OF THE House Mouse. Biol. Rev. Camb. Philos. Soc. *67*, 519–550. https://doi.org/10.1111/j.1469-185X.1992.tb01192.x.

52. Allen, K., Gonzalez-Olvera, R., Kumar, M., Feng, T., Pieraut, S., and Hoy, J.L. (2022). A binocular perception deficit characterizes prey pursuit in developing mice. iScience *25*, 105368. https://doi.org/10.1016/j.isci.2022.105368.

53. Hoy, J.L., Bishop, H.I., and Niell, C.M. (2019). Defined Cell Types in Superior Colliculus Make Distinct Contributions to Prey Capture Behavior in the Mouse. Curr. Biol. *29*, 4130–4138.e5. https://doi.org/10.1016/j.cub.2019.10.017.

54. Johnson, K.P., Fitzpatrick, M.J., Zhao, L., Wang, B., McCracken, S., Williams, P.R., and Kerschensteiner, D. (2021). Cell-type-specific binocular vision guides predation in mice. Neuron *109*, 1527–1539.e4. https://doi.org/10.1016/j.neuron.2021.03.010.

55. Barnes, S.J., Franzoni, E., Jacobsen, R.I., Erdelyi, F., Szabo, G., Clopath, C., Keller, G.B., and Keck, T. (2017). Deprivation-Induced Homeostatic Spine Scaling In Vivo Is Localized to Dendritic Branches that Have Undergone Recent Spine Loss. Neuron *96*, 871–882.e5. https://doi.org/10.1016/j.neuron.2017.09.052.

56. Wen, W., Prada, A.M., and Turrigiano, G.G. (2025). Modular arrangement of synaptic and intrinsic homeostatic plasticity within visual cortical circuits. Proc. Natl. Acad. Sci USA *122*, e2504775122. https://doi.org/10.1073/pnas.2504775122.

57. Mathis, A., Mamidanna, P., Cury, K.M., Abe, T., Murthy, V.N., Mathis, M.W., and Bethge, M. (2018). DeepLabCut: markerless pose estimation of user-defined body parts with deep learning. Nat. Neurosci. *21*, 1281–1289. https://doi.org/10.1038/s41593-018-0209-y.

58. Shield, S., Jericevich, R., Patel, A., and Jusufi, A. (2021). Tails, Flails, and Sails: How Appendages Improve Terrestrial Maneuverability by Improving Stability. Integr. Comp. Biol. *61*, 506–520. https://doi.org/10.1093/icb/icab108.

59. Zhao, Z.-D., Zhang, L., Xiang, X., Kim, D., Li, H., Cao, P., and Shen, W.L. (2023). Neurocircuitry of Predatory Hunting. Neurosci. Bull. *39*, 817–831. https://doi.org/10.1007/s12264-022-01018-1.

60. Roth, B.L. (2016). DREADDs for Neuroscientists. Neuron *89*, 683–694. https://doi.org/10.1016/j.neuron.2016.01.040.

61. Nahmani, M., and Turrigiano, G.G. (2014). Deprivation-Induced Strengthening of Presynaptic and Postsynaptic Inhibitory Transmission in Layer 4 of Visual Cortex during the Critical Period. J. Neurosci. *34*, 2571–2582. https://doi.org/10.1523/JNEUROSCI.4600-13.2014.

62. Feng, G., Mellor, R.H., Bernstein, M., Keller-Peck, C., Nguyen, Q.T., Wallace, M., Nerbonne, J.M., Lichtman, J.W., and Sanes, J.R. (2000). Imaging Neuronal Subsets in Transgenic Mice Expressing Multiple Spectral Variants of GFP. Neuron *28*, 41–51. https://doi.org/10.1016/S0896-6273(00)00084-2.

63. Matsuzaki, M., Ellis-Davies, G.C.R., Nemoto, T., Miyashita, Y., Iino, M., and Kasai, H. (2001). Dendritic spine geometry is critical for AMPA receptor expression in hippocampal CA1 pyramidal neurons. Nat. Neurosci. *4*, 1086–1092. https://doi.org/10.1038/nn736.

64. Noguchi, J., Nagaoka, A., Watanabe, S., Ellis-Davies, G.C.R., Kitamura, K., Kano, M., Matsuzaki, M., and Kasai, H. (2011). *In vivo* two-photon uncaging of glutamate revealing the structure–function relationships of dendritic spines in the neocortex of adult mice. J. Physiol. *589*, 2447–2457. https://doi.org/10.1113/jphysiol.2011.207100.

65. Berry, K.P., and Nedivi, E. (2016). Experience-Dependent Structural Plasticity in the Visual System. Annu. Rev. Vis. Sci. *2*, 17–35. https://doi.org/10.1146/annurev-vision-111815-114638.

66. Larkum, M. (2013). A cellular mechanism for cortical associations: an organizing principle for the cerebral cortex. Trends Neurosci. *36*, 141–151. https://doi.org/10.1016/j.tins.2012.11.006.

67. Wang, Y., Wu, W., Zhang, X., Hu, X., Li, Y., Lou, S., Ma, X., An, X., Liu, H., Peng, J., et al. (2016). A Mouse Model of Visual Perceptual Learning Reveals Alterations in Neuronal Coding and Dendritic Spine Density in the Visual Cortex. Front. Behav. Neurosci. *10*, 42. https://doi.org/10.3389/fnbeh.2016.00042.

68. Lopez-Ortega, E., Choi, J.Y., Hong, I., Roth, R.H., Cudmore, R.H., and Huganir, R.L. (2024). Stimulus-dependent synaptic plasticity underlies neuronal circuitry refinement in the mouse primary visual cortex. Cell Rep. *43*, 113966. https://doi.org/10.1016/j.celrep.2024.113966.

69. Hu, G., Chen, A., Ye, J., Liu, Q., Wang, J., Fan, C., Wang, X., Huang, M., Dai, M., Shi, X., et al. (2024). A developmental critical period for ocular dominance plasticity of binocular neurons in mouse superior colliculus. Cell Rep. *43*, 113667. https://doi.org/10.1016/j.celrep.2023.113667.

70. Su, J., Sabbagh, U., Liang, Y., Olejníková, L., Dixon, K.G., Russell, A.L., Chen, J., Pan, Y.A., Triplett, J.W., and Fox, M.A. (2021). A cell–ECM mechanism for connecting the ipsilateral eye to the brain. Proc. Natl. Acad. Sci. USA *118*, e2104343118. https://doi.org/10.1073/pnas.2104343118.

71. Langer, T.P., and Lund, R.D. (1974). The upper layers of the superior colliculus of the rat: A Golgi study. J. Comp. Neurol. *158*, 418–435. https://doi.org/10.1002/cne.901580404.

72. Matcham, A.C., Toma, K., Tsai, N.Y., Sze, C.J., Lin, P.-Y., Stewart, I.F., and Duan, X. (2024). Cadherin-13 Maintains Retinotectal Synapses via Transneuronal Interactions. J. Neurosci. *44*, e1310232023. https://doi.org/10.1523/JNEUROSCI.1310-23.2023.

73. Jiang, S., Honnuraiah, S., and Stuart, G.J. (2023). Characterization of primary visual cortex input to specific cell types in the superior colliculus. Front. Neuroanat. *17*, 1282941. https://doi.org/10.3389/fnana.2023.1282941.

74. Rudy, B., Fishell, G., Lee, S., and Hjerling-Leffler, J. (2011). Three groups of interneurons account for nearly 100% of neocortical GABAergic neurons. Dev. Neurobiol. *71*, 45–61. https://doi.org/10.1002/dneu.20853.

75. Tremblay, R., Lee, S., and Rudy, B. (2016). GABAergic Interneurons in the Neocortex: From Cellular Properties to Circuits. Neuron *91*, 260–292. https://doi.org/10.1016/j.neuron.2016.06.033.

76. Sommeijer, J.-P., and Levelt, C.N. (2012). Synaptotagmin-2 Is a Reliable Marker for Parvalbumin Positive Inhibitory Boutons in the Mouse Visual Cortex. PLOS One *7*, e35323. https://doi.org/10.1371/journal.pone.0035323.

77. Richards, D.A., Mateos, J.M., Hugel, S., De Paola, V., Caroni, P., Gähwiler, B.H., and McKinney, R.A. (2005). Glutamate induces the rapid formation of spine head protrusions in hippocampal slice cultures. Proc. Natl. Acad. Sci. USA *102*, 6166–6171. https://doi.org/10.1073/pnas.0501881102.

78. Vlachos, A., Becker, D., Jedlicka, P., Winkels, R., Roeper, J., and Deller, T. (2012). Entorhinal Denervation Induces Homeostatic Synaptic Scaling

of Excitatory Postsynapses of Dentate Granule Cells in Mouse Organotypic Slice Cultures. PLOS One *7*, e32883. https://doi.org/10.1371/journal.pone.0032883.

79. Wierenga, C.J., Ibata, K., and Turrigiano, G.G. (2005). Postsynaptic Expression of Homeostatic Plasticity at Neocortical Synapses. J. Neurosci. *25*, 2895–2905. https://doi.org/10.1523/JNEUROSCI.5217-04.2005.
80. Guerrero, A.A., and Turrigiano, G.G. (2025). Activity Deprivation Modulates the Shank3/Homer1/mGluR5 Signaling Pathway to Enable Synaptic Upscaling. J. Neurosci. *45*, e0807252025. https://doi.org/10.1523/JNEUROSCI.0807-25.2025.
81. Turrigiano, G.G., Leslie, K.R., Desai, N.S., Rutherford, L.C., and Nelson, S.B. (1998). Activity-dependent scaling of quantal amplitude in neocortical neurons. Nature *391*, 892–896. https://doi.org/10.1038/36103.
82. Lambo, M.E., and Turrigiano, G.G. (2013). Synaptic and Intrinsic Homeostatic Mechanisms Cooperate to Increase L2/3 Pyramidal Neuron Excitability during a Late Phase of Critical Period Plasticity. J. Neurosci. *33*, 8810–8819. https://doi.org/10.1523/JNEUROSCI.4502-12.2013.
83. Steinmetz, C.C., and Turrigiano, G.G. (2010). Tumor Necrosis Factor-α Signaling Maintains the Ability of Cortical Synapses to Express Synaptic Scaling. J. Neurosci. *30*, 14685–14690. https://doi.org/10.1523/JNEUROSCI.2210-10.2010.
84. Stellwagen, D., and Malenka, R.C. (2006). Synaptic scaling mediated by glial TNF-α. Nature *440*, 1054–1059. https://doi.org/10.1038/nature04671.
85. Prusky, G.T., and Douglas, R.M. (2004). Characterization of mouse cortical spatial vision. Vis. Res. *44*, 3411–3418. https://doi.org/10.1016/j.visres.2004.09.001.
86. Glickfeld, L.L., Histed, M.H., and Maunsell, J.H.R. (2013). Mouse Primary Visual Cortex Is Used to Detect Both Orientation and Contrast Changes. J. Neurosci. *33*, 19416–19422. https://doi.org/10.1523/JNEUROSCI.3560-13.2013.
87. Poort, J., Khan, A.G., Pachitariu, M., Nemri, A., Orsolic, I., Krupic, J., Bauza, M., Sahani, M., Keller, G.B., Mrsic-Flogel, T.D., et al. (2015). Learning Enhances Sensory and Multiple Non-sensory Representations in Primary Visual Cortex. Neuron *86*, 1478–1490. https://doi.org/10.1016/j.neuron.2015.05.037.
88. Jurjut, O., Georgieva, P., Busse, L., and Katzner, S. (2017). Learning Enhances Sensory Processing in Mouse V1 before Improving Behavior. J. Neurosci. *37*, 6460–6474. https://doi.org/10.1523/JNEUROSCI.3485-16.2017.
89. Resulaj, A., Ruediger, S., Olsen, S.R., and Scanziani, M. (2018). First spikes in visual cortex enable perceptual discrimination. eLife *7*, e34044. https://doi.org/10.7554/eLife.34044.
90. Ruediger, S., and Scanziani, M. (2020). Learning speed and detection sensitivity controlled by distinct cortico-fugal neurons in visual cortex. eLife *9*, e59247. https://doi.org/10.7554/eLife.59247.
91. Mederos, S., Blakely, P., Vissers, N., Clopath, C., and Hofer, S.B. (2025). Overwriting an instinct: Visual cortex instructs learning to suppress fear responses. Science *387*, 682–688. https://doi.org/10.1126/science.adr2247.
92. Branco, T., and Redgrave, P. (2020). The Neural Basis of Escape Behavior in Vertebrates. Annu. Rev. Neurosci. *43*, 417–439. https://doi.org/10.1146/annurev-neuro-100219-122527.
93. Cai, P., Chen, L., Guo, Y.-R., Yao, J., Chen, H.-Y., Lu, Y.-P., Huang, S.-N., He, P., Zheng, Z.-H., Liu, J.-Y., et al. (2020). Basal forebrain GABAergic neurons promote arousal and predatory hunting. Neuropharmacology *180*, 108299. https://doi.org/10.1016/j.neuropharm.2020.108299.
94. Zhao, Z.D., Chen, Z., Xiang, X., Hu, M., Xie, H., Jia, X., Cai, F., Cui, Y., Chen, Z., Qian, L., et al. (2019). Zona incerta GABAergic neurons integrate prey-related sensory signals and induce an appetitive drive to promote hunting. Nat. Neurosci. *22*, 921–932. https://doi.org/10.1038/s41593-019-0404-5.
95. Bian, W.-J., Miao, W.-Y., He, S.-J., Qiu, Z., and Yu, X. (2015). Coordinated Spine Pruning and Maturation Mediated by Inter-Spine Competition for Cadherin/Catenin Complexes. Cell *162*, 808–822. https://doi.org/10.1016/j.cell.2015.07.018.
96. Lupori, L., Cornuti, S., Mazziotti, R., Borghi, E., Ottaviano, E., Cas, M.D., Sagona, G., Pizzorusso, T., and Tognini, P. (2022). The gut microbiota of environmentally enriched mice regulates visual cortical plasticity. Cell Rep. *38*, 110212. https://doi.org/10.1016/j.celrep.2021.110212.
97. Baroncelli, L., Braschi, C., Spolidoro, M., Begenisic, T., Sale, A., and Maffei, L. (2010). Nurturing brain plasticity: impact of environmental enrichment. Cell Death Differ. *17*, 1092–1103. https://doi.org/10.1038/cdd.2009.193.
98. Greifzu, F., Kalogeraki, E., and Löwel, S. (2016). Environmental enrichment preserved lifelong ocular dominance plasticity, but did not improve visual abilities. Neurobiol. Aging *41*, 130–137. https://doi.org/10.1016/j.neurobiolaging.2016.02.014.
99. Kempermann, G. (2019). Environmental enrichment, new neurons and the neurobiology of individuality. Nat. Rev. Neurosci. *20*, 235–245. https://doi.org/10.1038/s41583-019-0120-x.
100. Procacci, N.M., Allen, K.M., Robb, G.E., Ijekah, R., Lynam, H., and Hoy, J.L. (2020). Context-dependent modulation of natural approach behaviour in mice. Proc. Biol. Sci. *287*, 20201189. https://doi.org/10.1098/rspb.2020.1189.
101. Cang, J., Fu, J., and Tanabe, S. (2023). Neural circuits for binocular vision: Ocular dominance, interocular matching, and disparity selectivity. Front. Neural Circuits *17*, 1084027. https://doi.org/10.3389/fncir.2023.1084027.
102. Priebe, N.J. (2016). Mechanisms of Orientation Selectivity in the Primary Visual Cortex. Annu. Rev. Vis. Sci. *2*, 85–107. https://doi.org/10.1146/annurev-vision-111815-114456.
103. Niell, C.M., and Scanziani, M. (2021). How Cortical Circuits Implement Cortical Computations: Mouse Visual Cortex as a Model. Annu. Rev. Neurosci. *44*, 517–546. https://doi.org/10.1146/annurev-neuro-102320-085825.
104. Li, Y., Fitzpatrick, D., and White, L.E. (2006). The development of direction selectivity in ferret visual cortex requires early visual experience. Nat. Neurosci. *9*, 676–681. https://doi.org/10.1038/nn1684.
105. Ritter, N.J., Anderson, N.M., and Van Hooser, S.D. (2017). Visual Stimulus Speed Does Not Influence the Rapid Emergence of Direction Selectivity in Ferret Visual Cortex. J. Neurosci. *37*, 1557–1567. https://doi.org/10.1523/JNEUROSCI.3365-16.2016.
106. Griswold, S.V., and Van Hooser, S.D. (2025). Premature vision drives aberrant development of response properties in primary visual cortex. eLife *14*, RP106513. https://doi.org/10.7554/eLife.106513.
107. Kalogeraki, E., Pielecka-Fortuna, J., and Löwel, S. (2017). Environmental enrichment accelerates ocular dominance plasticity in mouse visual cortex whereas transfer to standard cages resulted in a rapid loss of increased plasticity. PLOS One *12*, e0186999. https://doi.org/10.1371/journal.pone.0186999.
108. Xu, T., Yu, X., Perlik, A.J., Tobin, W.F., Zweig, J.A., Tennant, K., Jones, T., and Zuo, Y. (2009). Rapid formation and selective stabilization of synapses for enduring motor memories. Nature *462*, 915–919. https://doi.org/10.1038/nature08389.
109. Yang, Y., Liu, D.Q., Huang, W., Deng, J., Sun, Y., Zuo, Y., and Poo, M.M. (2016). Selective synaptic remodeling of amygdalocortical connections associated with fear memory. Nat. Neurosci. *19*, 1348–1355. https://doi.org/10.1038/nn.4370.
110. Keifer, O.P., Jr., Hurt, R.C., Gutman, D.A., Keilholz, S.D., Gourley, S.L., and Ressler, K.J. (2015). Voxel-based morphometry predicts shifts in dendritic spine density and morphology with auditory fear conditioning. Nat. Commun. *6*, 7582. https://doi.org/10.1038/ncomms8582.

111. Xu, Z., Adler, A., Li, H., Pérez-Cuesta, L.M., Lai, B., Li, W., and Gan, W.-B. (2019). Fear conditioning and extinction induce opposing changes in dendritic spine remodeling and somatic activity of layer 5 pyramidal neurons in the mouse motor cortex. Sci. Rep. *9*, 4619. https://doi.org/10.1038/s41598-019-40549-y.

112. Lai, C.S.W., Franke, T.F., and Gan, W.-B. (2012). Opposite effects of fear conditioning and extinction on dendritic spine remodelling. Nature *483*, 87–91. https://doi.org/10.1038/nature10792.

113. Caroni, P., Donato, F., and Muller, D. (2012). Structural plasticity upon learning: regulation and functions. Nat. Rev. Neurosci. *13*, 478–490. https://doi.org/10.1038/nrn3258.

114. Hofer, S.B., Mrsic-Flogel, T.D., Bonhoeffer, T., and Hübener, M. (2009). Experience leaves a lasting structural trace in cortical circuits. Nature *457*, 313–317. https://doi.org/10.1038/nature07487.

115. Keck, T., Keller, G.B., Jacobsen, R.I., Eysel, U.T., Bonhoeffer, T., and Hübener, M. (2013). Synaptic Scaling and Homeostatic Plasticity in the Mouse Visual Cortex In Vivo. Neuron *80*, 327–334. https://doi.org/10.1016/j.neuron.2013.08.018.

116. Barnes, S.J., Sammons, R.P., Jacobsen, R.I., Mackie, J., Keller, G.B., and Keck, T. (2015). Subnetwork-Specific Homeostatic Plasticity in Mouse Visual Cortex In Vivo. Neuron *86*, 1290–1303. https://doi.org/10.1016/j.neuron.2015.05.010.

117. Jenks, K.R., and Shepherd, J.D. (2020). Experience-Dependent Development and Maintenance of Binocular Neurons in the Mouse Visual Cortex. Cell Rep. *30*, 1982–1994.e4. https://doi.org/10.1016/j.celrep.2020.01.031.

118. Lehmann, K., and Löwel, S. (2008). Age-Dependent Ocular Dominance Plasticity in Adult Mice. PLOS One *3*, e3120. https://doi.org/10.1371/journal.pone.0003120.

119. Heynen, A.J., Yoon, B.-J., Liu, C.-H., Chung, H.J., Huganir, R.L., and Bear, M.F. (2003). Molecular mechanism for loss of visual cortical responsiveness following brief monocular deprivation. Nat. Neurosci. *6*, 854–862. https://doi.org/10.1038/nn1100.

120. Kaneko, M., Stellwagen, D., Malenka, R.C., and Stryker, M.P. (2008). Tumor Necrosis Factor-α Mediates One Component of Competitive, Experience-Dependent Plasticity in Developing Visual Cortex. Neuron *58*, 673–680. https://doi.org/10.1016/j.neuron.2008.04.023.

121. Ranson, A., Cheetham, C.E.J., Fox, K., and Sengpiel, F. (2012). Homeostatic plasticity mechanisms are required for juvenile, but not adult, ocular dominance plasticity. Proc. Natl. Acad. Sci. USA *109*, 1311–1316. https://doi.org/10.1073/pnas.1112204109.

122. Dringenberg, H.C. (2020). The history of LONG-TERM potentiation as a memory mechanism: Controversies, confirmation, and some lessons to remember. Hippocampus *30*, 987–1012. https://doi.org/10.1002/hipo.23213.

123. Mendez, P., Stefanelli, T., Flores, C.E., Muller, D., and Lüscher, C. (2018). Homeostatic Plasticity in the Hippocampus Facilitates Memory Extinction. Cell Rep. *22*, 1451–1461. https://doi.org/10.1016/j.celrep.2018.01.025.

124. Wu, C.-H., Ramos, R., Katz, D.B., and Turrigiano, G.G. (2021). Homeostatic synaptic scaling establishes the specificity of an associative memory. Curr. Biol. *31*, 2274–2285.e5. https://doi.org/10.1016/j.cub.2021.03.024.

125. Chen, T.-W., Wardill, T.J., Sun, Y., Pulver, S.R., Renninger, S.L., Baohan, A., Schreiter, E.R., Kerr, R.A., Orger, M.B., Jayaraman, V., et al. (2013). Ultrasensitive fluorescent proteins for imaging neuronal activity. Nature *499*, 295–300. https://doi.org/10.1038/nature12354.

126. Krashes, M.J., Koda, S., Ye, C., Rogan, S.C., Adams, A.C., Cusher, D.S., Maratos-Flier, E., Roth, B.L., and Lowell, B.B. (2011). Rapid, reversible activation of AgRP neurons drives feeding behavior in mice. J. Clin. Investig. *121*, 1424–1428. https://doi.org/10.1172/JCI46229.

127. Madisen, L., Zwingman, T.A., Sunkin, S.M., Oh, S.W., Zariwala, H.A., Gu, H., Ng, L.L., Palmiter, R.D., Hawrylycz, M.J., Jones, A.R., et al. (2010). A robust and high-throughput Cre reporting and characterization system for the whole mouse brain. Nat. Neurosci. *13*, 133–140. https://doi.org/10.1038/nn.2467.

128. Hippenmeyer, S., Vrieseling, E., Sigrist, M., Portmann, T., Laengle, C., Ladle, D.R., and Arber, S. (2005). A Developmental Switch in the Response of DRG Neurons to ETS Transcription Factor Signaling. PLOS Biol. *3*, e159. https://doi.org/10.1371/journal.pbio.0030159.

129. Nath, T., Mathis, A., Chen, A.C., Patel, A., Bethge, M., and Mathis, M.W. (2019). Using DeepLabCut for 3D markerless pose estimation across species and behaviors. Nat. Protoc. *14*, 2152–2176. https://doi.org/10.1038/s41596-019-0176-0.

130. Pachitariu, M., Stringer, C., Dipoppa, M., Schröder, S., Rossi, L.F., Dalgleish, H., Carandini, M., and Harris, K.D. (2017). Suite2p: beyond 10,000 neurons with standard two-photon microscopy. Preprint at bioRxiv. https://doi.org/10.1101/061507.

131. Holtmaat, A., Bonhoeffer, T., Chow, D.K., Chuckowree, J., De Paola, V., Hofer, S.B., Hübener, M., Keck, T., Knott, G., Lee, W.-C.A., et al. (2009). Long-term, high-resolution imaging in the mouse neocortex through a chronic cranial window. Nat. Protoc. *4*, 1128–1144. https://doi.org/10.1038/nprot.2009.89.

132. Lewitus, G.M., Pribiag, H., Duseja, R., St-Hilaire, M., and Stellwagen, D. (2014). An Adaptive Role of TNFα in the Regulation of Striatal Synapses. J. Neurosci. *34*, 6146–6155. https://doi.org/10.1523/JNEUROSCI.3481-13.2014.

133. Yli-Karjanmaa, M., Larsen, K.S., Fenger, C.D., Kristensen, L.K., Martin, N.A., Jensen, P.T., Breton, A., Nathanson, L., Nielsen, P.V., Lund, M.C., et al. (2019). TNF deficiency causes alterations in the spatial organization of neurogenic zones and alters the number of microglia and neurons in the cerebral cortex. Brain Behav. Immun. *82*, 279–297. https://doi.org/10.1016/j.bbi.2019.08.195.

134. Burgess, C.P., Lak, A., Steinmetz, N.A., Zatka-Haas, P., Bai Reddy, C., Jacobs, E.A.K., Linden, J.F., Paton, J.J., Ranson, A., Schröder, S., et al. (2017). High-Yield Methods for Accurate Two-Alternative Visual Psychophysics in Head-Fixed Mice. Cell Rep. *20*, 2513–2524. https://doi.org/10.1016/j.celrep.2017.08.047.

135. Brainard, D.H. (1997). The Psychophysics Toolbox. Spat. Vis. *10*, 433–436. https://doi.org/10.1163/156856897X00357.

136. Kleiner, M., Brainard, D.H., and Pelli, D.G. (2007). What's new in Psychtoolbox-3? Perception *36*, 14.

137. Pelli, D.G. (1997). The VideoToolbox software for visual psychophysics: transforming numbers into movies. Spat. Vis. *10*, 437–442. https://doi.org/10.1163/156856897X00366.

138. Mazurek, M., Kager, M., and Van Hooser, S.D. (2014). Robust quantification of orientation selectivity and direction selectivity. Front. Neural Circuits *8*, 92. https://doi.org/10.3389/fncir.2014.00092.

139. Ringach, D.L., Shapley, R.M., and Hawken, M.J. (2002). Orientation Selectivity in Macaque V1: Diversity and Laminar Dependence. J. Neurosci. *22*, 5639–5651. https://doi.org/10.1523/JNEUROSCI.22-13-05639.2002.

140. Albrecht, D.G., and Hamilton, D.B. (1982). Striate cortex of monkey and cat: contrast response function. J. Neurophysiol. *48*, 217–237. https://doi.org/10.1152/jn.1982.48.1.217.

141. Naka, K.I., and Rushton, W.A.H. (1966). S-potentials from colour units in the retina of fish (Cyprinidae). J. Physiol. *185*, 536–555. https://doi.org/10.1113/jphysiol.1966.sp008001.

142. Peirce, J.W. (2007). The potential importance of saturating and supersaturating contrast response functions in visual cortex. J. Vis. *7*, 13. https://doi.org/10.1167/7.6.13.

143. Enroth-Cugell, C., and Robson, J.G. (1966). The contrast sensitivity of retinal ganglion cells of the cat. J. Physiol. *187*, 517–552. https://doi.org/10.1113/jphysiol.1966.sp008107.

144. Heimel, J.A., Van Hooser, S.D., and Nelson, S.B. (2005). Laminar Organization of Response Properties in Primary Visual Cortex of the

Gray Squirrel (*Sciurus carolinensis*). J. Neurophysiol. *94*, 3538–3554. https://doi.org/10.1152/jn.00106.2005.

145. Movshon, J.A., Kiorpes, L., Hawken, M.J., and Cavanaugh, J.R. (2005). Functional Maturation of the Macaque's Lateral Geniculate Nucleus. J. Neurosci. *25*, 2712–2722. https://doi.org/10.1523/JNEUROSCI.2356-04.2005.

146. Andermann, M.L., Kerlin, A.M., Roumis, D.K., Glickfeld, L.L., and Reid, R.C. (2011). Functional Specialization of Mouse Higher Visual Cortical Areas. Neuron *72*, 1025–1039. https://doi.org/10.1016/j.neuron.2011.11.013.

147. Wen, W., and Turrigiano, G.G. (2021). Developmental Regulation of Homeostatic Plasticity in Mouse Primary Visual Cortex. J. Neurosci. *41*, 9891–9905. https://doi.org/10.1523/JNEUROSCI.1200-21.2021.

148. Pnevmatikakis, E.A., and Giovannucci, A. (2017). NoRMCorre: An online algorithm for piecewise rigid motion correction of calcium imaging data. J. Neurosci. Methods *291*, 83–94. https://doi.org/10.1016/j.jneumeth.2017.07.031.

149. Scholl, B., Thomas, C.I., Ryan, M.A., Kamasawa, N., and Fitzpatrick, D. (2021). Cortical response selectivity derives from strength in numbers of synapses. Nature *590*, 111–114. https://doi.org/10.1038/s41586-020-03044-3.

150. Schindelin, J., Arganda-Carreras, I., Frise, E., Kaynig, V., Longair, M., Pietzsch, T., Preibisch, S., Rueden, C., Saalfeld, S., Schmid, B., et al. (2012). Fiji: an open-source platform for biological-image analysis. Nat. Methods *9*, 676–682. https://doi.org/10.1038/nmeth.2019.

151. Gale, S.D., and Murphy, G.J. (2014). Distinct Representation and Distribution of Visual Information by Specific Cell Types in Mouse Superficial Superior Colliculus. J. Neurosci. *34*, 13458–13471. https://doi.org/10.1523/JNEUROSCI.2768-14.2014.

152. Porrero, C., Rubio-Garrido, P., Avendaño, C., and Clascá, F. (2010). Mapping of fluorescent protein-expressing neurons and axon pathways in adult and developing Thy1-eYFP-H transgenic mice. Brain Res. *1345*, 59–72. https://doi.org/10.1016/j.brainres.2010.05.061.

153. Schuett, S., Bonhoeffer, T., and Hübener, M. (2002). Mapping Retinotopic Structure in Mouse Visual Cortex with Optical Imaging. J. Neurosci. *22*, 6549–6559. https://doi.org/10.1523/JNEUROSCI.22-15-06549.2002.

154. Wen, W., Prada, A.M., and Turrigiano, G.G. (2025). Modular Arrangement of Synaptic and Intrinsic Homeostatic Plasticity within Visual Cortical Circuits. Proc. Natl. Acad. Sci. USA *122*, e2504775122. https://doi.org/10.1073/pnas.2504775122.

Please cite this article in press as: Bissen et al., Ethological learning during the critical period resets synaptic setpoints in mouse binocular visual cortex, Neuron (2026), https://doi.org/10.1016/j.neuron.2026.06.016

STAR★METHODS

KEY RESOURCES TABLE

REAGENT OR RESOURCE	SOURCE	IDENTIFIER
Antibodies		
Rabbit polyclonal anti-GFP	ThermoFisher	RRID: AB_221569
Chicken polyclonal anti-GFP	Millipore	RRID: AB_90890
Rabbit polyclonal anti-NeuN	ThermoFisher	RRID: AB_2736207
Mouse monoclonal anti-NeuN	Millipore	RRID: AB_2298772
Mouse monoclonal anti-Syt2	Developmental Studies Hybridoma Bank (DSHB)	RRID: AB_2315626
Rat monoclonal anti-SST	Sigma Aldrich	RRID: AB_2255365
Rabbit polyclonal anti-VGAT	Synaptic Systems	RRID: AB_887869
Chicken polyclonal anti-PV	Synaptic Systems	RRID: AB_2619887
Rat monoclonal anti-mCherry	ThermoFisher	RRID: AB_2536611
Rabbit monoclonal anti-cFos	Cell Signaling Technologies	RRID: AB_2298772
Goat polyclonal anti-chicken Alexa 488	ThermoFisher	RRID: AB_2534096
Goat polyclonal anti-chicken Alexa 568	ThermoFisher	RRID: AB_2534098
Goat polyclonal anti-rabbit Alexa 488	ThermoFisher	RRID: AB_143165
Goat polyclonal anti-rabbit Alexa 568	ThermoFisher	RRID: AB_143157
Goat polyclonal anti-rabbit Alexa 647	ThermoFisher	RRID: AB_2535812
Goat polyclonal anti-mouse Alexa 647	ThermoFisher	RRID: AB_2535804
Goat polyclonal anti-mouse Alexa 405	ThermoFisher	RRID: AB_2890536
Goat polyclonal anti-rat Alexa 568	ThermoFisher	RRID: AB_2534121
Bacterial and virus strains		
AAV9.Syn.GCaMP6s.WPRE.SV40	Chen et al.[125]	Addgene: 100843-AAV9
AAV9.hSyn.DIO.hM3D(Gq).mCherry	Krashes et al.[126]	Addgene: 44361-AAV9
Chemicals, peptides and recombinant proteins		
XPro1595	INmune Bio	N/A
Clozapine-N-Oxide (CNO)	HelloBio	N/A
C&B Metabond	Parkell	Cat# S380
Clarity Ultrasound Gel	Aurora	Cat # 59007
Experimental models: Organisms/strains		
Mouse: B6.Cg-Tg(Thy1-YFP)HJrs/J	Feng et al.[62]	RRID: IMSR_JAX:003782
Mouse: B6.Cg-Gt(ROSA)26Sortm14 (CAG-tdTomato)Hze/J	Madisen et al.[127]	RRID: IMSR_JAX:007914
Mouse: B6;C3-Tg(Scnn1a-cre)3Aibs/J	Madisen et al.[127]	RRID: IMSR_JAX:009613
Mouse: B6;129P2-Pvalbtm1(cre)Arbr/J	Hippenmeyer et al.[128]	RRID: IMSR_JAX:008069
Software and algorithms		
Huygens Essential	Scientific Volume Imaging	RRID: SCR_014237
ImageJ/Fiji	Fiji	RRID: SCR_002285
Imaris	Oxford Instruments	RRID: SCR_007370
DeepLabCut	Mathis et al.[57]; Nath et al.[129]	RRID: SCR_021391
GraphPad	Prism	RRID: SCR_002798
Matlab	MathWorks	RRID: SCR_001622
Suite2p	Pachitariu et al.[130]	RRID: SCR_016434
Illustrator	Adobe	RRID: SCR_010279
Photoshop	Adobe	RRID: SCR_014199

(*Continued on next page*)

Please cite this article in press as: Bissen et al., Ethological learning during the critical period resets synaptic setpoints in mouse binocular visual cortex, Neuron (2026), https://doi.org/10.1016/j.neuron.2026.06.016

Continued

REAGENT OR RESOURCE	SOURCE	IDENTIFIER
Brandeis Light Microscopy Core Facility	Brandeis University	RRID: SCR_025892
Subcellular registration for spine imaging	This manuscript	github.com/kasailor /AwakeImgStbl; 10.5281/zenodo.20610220
Custom MATLAB software for behavioral analysis	This manuscript	github.com/turrigiano CodeSpace/Bissen2025; 10.5281/zenodo.20614271
Calcium imaging analysis	Van Hooser lab	github.com/VH-Lab/vhlab-TwoPhoton-matlab RRID: SCR_023369; 10.5281/zenodo.20601922
Nested and effect size analysis	This manuscript	github.com/VH-Lab/vhtlab -mousehunting-matlab; 10.5281/zenodo.20601930

EXPERIMENTAL MODEL AND STUDY PARTICIPANT DETAILS

Animals

All procedures were approved by the Institutional Biosafety Committee and the Institutional Animal Care and Use Committee at Brandeis University, and performed in compliance with the National Institutes of Health Guide for the Care and Use of Laboratory Animals. Thy1-YFP line H (B6.Cg-Tg(Thy1-YFP)HJrs/J), Ai14 (B6.Cg-Gt(ROSA)26Sortm14(CAG-tdTomato)Hze/J), SCN1-Cre (B6;C3-Tg(Scnn1a-cre)3Aibs/J) and PV-Cre (B6;129P2-Pvalbtm1(cre)Arbr/J) mice were housed on a 12/12 light/dark cycle in a dedicated, climate-controlled facility. Thy1-YFP mice express the yellow fluorescent protein (YFP) in a subset of L5 and L2/3 pyramidal neurons and were used for all experiments except calcium imaging experiments (i.e. all but Figures 2, S2, and 7F–7H), as the endogenous YFP expression interferes with GCaMP imaging. Thy1-YFP were crossed to PV-Cre mice for the chemogenetic inactivation of V1 and the subsequent analysis of behavioral and structural phenotypes (Figures 8 and S8). Ai14 or SCN1-Cre^{-} mice were used for calcium imaging; no difference was observed between these strains and thus data were pooled. Unless stated otherwise, food and water were available *ad libitum*, and animals were raised normally and housed in groups of 2–5 after weaning. Littermates of both sexes were randomly allocated to experimental groups. Two age ranges were used: for critical period experiments (Figures 1, 2, 3, 4, 5, 6, 7, and 8) hunting sessions occurred between P28-P35, while for young adult mice they occurred between P44-52.

METHOD DETAILS

Prey capture learning paradigm

Prey capture learning was performed using a modification of the procedures in Groves Kuhnle et al. (2022).[49] For 5–9 days prior to the start of the prey capture paradigm (P19-P21 for critical-period mice, P34-P39 for adults), mice were moved to a separate dedicated housing facility and housed in a custom-made cage (150in^2) divided in two equal halves by a divider with regularly spaced holes, so that the mice would be single-housed in their own half while having access to a social partner of the same litter. Housing cages were placed halfway on a heating pad (medium setting). Cedar chip bedding (Beta Chip and Enviro Dri, Shepherd), standard chow and water were provided. Mice were weighed daily and monitored for health indicators. The 14x14in acrylic hunting arena was covered with absorbent underpads (Fisherbrand) taped down along the sides; underpads were only changed during the paradigm if necessary due to soiling. Two arenas (hunting and mock) were available in the dedicated room. The hunting arena was equipped with custom 3D printed, motorized, remote-controlled cricket dispensers. These were loaded with 10 live crickets prior to the start of each hunting session and automatically dispensed one cricket at a time via an Arduino motor system controlled remotely by the experimenter. In the mock arena, immobilized crickets (without head or legs) were dispensed manually to random locations, to prevent a learned association between dispenser drop sites and cricket locations. Arenas were illuminated from above with an additional white LED ring and behavior was recorded from above using a Logitech C922 HD Pro Stream Webcam (640 x 480 pixels) with Synapse (TDT) software for the hunting arena (20 frames per second, fps), or with the built-in Windows camera software (30 fps) for the mock arena.

For two days prior to the first hunting/mock session, mice were habituated to the hunting or mock arena for one 60 min-long session per day for two days. Halfway through, they were given an immobilized cricket to habituate them to cricket smell and taste and to reduce neophobia. Mice were food deprived for up to 16 h prior to the start of each hunting/mock session to minimize variability in motivation and appetitive drive, but had water *ad libitum*. Mice then underwent three days of hunting/mock with one session per day (days 1–3), followed by two days with no hunting/mock session (days 4–5) and one last day with one hunting/mock session (day 6). For critical-period mice, all hunting/mock sessions took place over the course of 6 days between P28 and P35, with the first session taking place on P28-P30. For adult mice, all hunting sessions took place over the course of 6 days between P44 and P52, with the first session taking place on P44-P47. Food pellets were provided at the end of each hunting/mock session and mice always regained the weight lost during the previous night of food deprivation.

Please cite this article in press as: Bissen et al., Ethological learning during the critical period resets synaptic setpoints in mouse binocular visual cortex, Neuron (2026), https://doi.org/10.1016/j.neuron.2026.06.016

Hunting/mock sessions were started immediately after the lights turned on (9:00 am) and included up to 3 successive mice, run through the paradigm in the same order on successive days. Each hunting or mock session comprised 10 crickets; during the first session mice occasionally ignored crickets, and these were removed if they were not captured/consumed within 15 min. Each cricket was dispensed at least 1 min after the end of the consumption of the previous cricket. For each mock session, 10 immobilized crickets were dispensed individually at regular intervals to replicate the average length of a hunting session on the same day (day 1, 2, 3 or 6). Animals were sacrificed a minimum 3 h after the last hunting session on day 6 to match the timing of perfusion after *in vivo* imaging, or 75min for cFos staining or electrophysiological recordings. Some critical-period mice were sacrificed 3 h after the first hunting/mock session to provide an earlier timepoint for large-scale dendritic imaging. A subset of the animals used for the behavior for Figure 1 were also used to analyze structural plasticity in Figures 3, 4, and 5.

Cranial window surgery and GCaMP6s virus injection

For *in vivo* imaging experiments in critical-period mice, a cranial window was placed over the binocular visual cortex (V1b) in the right hemisphere as previously described.[131] Briefly, mice were anesthetized using isoflurane (3% for induction, 1.8% on the stereotaxic frame, steadily decreased until 0.8% by the end of the surgery) and administered a single dose of dexamethasone sodium phosphate (2mg/kg body weight i.m.) and meloxicam (2–5mg/kg body weight i.p.) prior to surgery. Glass coverslips plugs were prepared in advance with a bottom coverslip of 2mm diameter (custom-made by Potomac Photonics) and a top coverslip of 3 mm diameter (#1, Warner Instruments), glued with index-matched adhesive (Norland #71). A cranial window of 2mm in diameter was carefully drilled above V1b (centered 3mm from the midline, 1mm anterior to lambda) and a glass coverslip plug was lowered into the window until the top coverslip was flushed against the skull. This configuration minimizes brain motion for awake imaging in head-fixed mice. The coverslip plug was then fixed to the skull using dental cement (C&B Metabond, Parkell) and a custom-made headplate was subsequently affixed to it, also using dental cement. Mice received dexamethasone sodium phosphate and meloxicam every 24h for 48h after surgery, and weight and general health signs were monitored daily. Mice were allowed recovery for at least 72h prior to the first habituation to the imaging restraint.

For calcium imaging experiments, mice were also injected with AAV9-GCaMP6s (the plasmid pAAV.CAG.GCaMP6s.WPRE.SV40 was a gift from Douglas Kim and the GENIE project to Addgene, which provided the viral prep in AAV9 at $\sim 1x10^{13}$ vg/ml; Addgene viral prep #100843-AAV9) after the cranial window was drilled, but before the glass coverslip was inserted. Up to 4 injections (350 nl at 1:3 dilution in 0.9% sterile saline) were made at 250 μm deep around the edges of the craniotomy while avoiding large blood vessels. The brain was kept humid using sterile saline between injections.

XPro51595 administration

The small molecule tumor necrosis factor alpha (TNFα) inhibitor XPro1595 was injected as described previously.[55,56] XPro1595 was dissolved in 0.9 % sterile saline at 1 mg/ml and administered subcutaneously at 10 mg/kg body weight. As XPro1595 action has been reported to last,[15,48–71,132,133] either XPro1595 or saline control was injected twice to ensure a long-lasting block of TNFα-dependent plasticity after learning: the first injection 1 h after the end of the first hunting/mock session, and the second roughly halfway through the paradigm, i.e. at 9:00 pm on day 3. For XPro behavioral experiments, the control cohort consisted of non-injected (n=5) and saline-injected (n=3) mice; these two cohorts had similar learning curves (Figures S8L and S8M) and were therefore combined.

Chemogenetic experiments and CNO injection

For chemogenetic experiments, Thy1-YFP x PV-Cre mice of both genotypes (Thy1-YFP +; PV-Cre + and Thy1-YFP+; PV-Cre -) were injected at P19-P21 with the cre-dependent excitatory DREADD AAV9-hSyn-DIO- hM3D(Gq)-mCherry (the plasmid was a gift from Bryan Roth; Addgene viral prep #44361-AAV9). Briefly, mice were anesthetized using isoflurane (3% for induction, 1.8% on the stereotaxic frame, steadily decreased until 0.8% by the end of the surgery) and administered a single dose of meloxicam (2–5mg/kg body weight i.p.) before surgery. The visual cortex was targeted using Allen Brain Atlas coordinates adjusted for lambda-delta distance and a single injection (300–350nl, undiluted) was made at 350μm deep. Mice received meloxicam 24h after surgery, and weight and general health signs were monitored daily until the end of the experiment. Mice recovered at least a week before the start of behavioral experiments.

Clozapine N-Oxide (CNO, HelloBio) was diluted in 0.9% sterile saline to reach a concentration of 1mg/mL and was administered subcutaneously at 10mg/kg body weight, 45min prior to the start of each hunting session, to mice of both genotypes (Thy1-YFP +; PV-Cre + and Thy1-YFP+; PV-Cre -). Mice were habituated to the process by daily injections of sterile saline for at least 5 days prior to the start of the experiment.

In vivo imaging

Starting at least 72 h after surgery, mice were progressively habituated to a custom-made restraint in 15 min increments until a maximal duration of 60 min. The restraint was a hemispherical tube of black Delrin with various covers to adjust for differences in animal size as they develop, and included a small wheel in the front for animals to grasp for distraction (based on[134]). All *in vivo* imaging was performed in awake, head-fixed, critical-period mice using an Ultima Plus two-photon microscope (Bruker), with a 16x water-dipping objective (NA 0.8, Nikon).

Please cite this article in press as: Bissen et al., Ethological learning during the critical period resets synaptic setpoints in mouse binocular visual cortex, Neuron (2026), https://doi.org/10.1016/j.neuron.2026.06.016

For chronic two-photon spine imaging, apical dendritic segments of L5 pyramidal neuron dendrites in layer 1 were imaged. Regions of interest were drawn around dendritic segments and images were acquired as Z-stacks using a resonant scanner at 15 kHz at 920nm at 920nm and less than 50 mW of laser power to avoid phototoxicity. Because water evaporates due to laser heat, the objective was immersed in a water-based ultrasound gel (Aurora) to enable uninterrupted imaging sessions. Bright dendritic segments were selected on the first imaging session (day 0, after the second habituation to the hunting/mock arena). One to three dendritic segments were acquired per neuron, and one to two neurons were imaged per animal. These segments were subsequently imaged each day and identified by landmarks (blood vessels) and neuronal morphology (dendritic branch point). Dendritic segments whose brightness decreased over time were excluded from the analysis.

For calcium imaging, mice were exposed to four batteries of visual stimuli to assess various receptive field properties during one imaging session after the last hunting/mock session (on the same day or the following day). Stimuli were shown on an HD monitor (1920 x 1080 pixels) placed 40 cm from the mouse, with the mouse facing the center of the monitor, at reduced brightness (64 64 64). Calcium responses were acquired at 180–250 μm depth below the pial surface (within layer 2/3) imaged at 1Hz with less than 50mW laser power. We assessed direction and spatial or temporal frequency tuning by presenting 8 directions (0–360° at 45° intervals) at 5 spatial frequencies (evenly spaced between 0.01 and 0.32 cycles/degree, cpd) or at 5 temporal frequencies (1, 2, 4, 8 or 16 Hz). Contrast sensitivity was calculated by showing 7 spatial frequencies (evenly spaced between 0.01 and 0.32 cpd) at 5 different contrasts (evenly spaced between 16% and 100%). Finally, we also measured binocular matching by presenting 8 directions (0–360° at 45° intervals) at one spatial frequency (0.02 cpd) with both eyes uncovered, or with the contralateral (left) or ipsilateral (right) eye covered. For each stimulus, full-screen sinusoidal rectangular gratings were drifting for a total duration of 2 s. Stimuli were separated by 5 s of blank screen. Within each battery, each combination was shown five times and stimuli (including blank) were all presented in a random order. Stimuli were computed using the Psychophysics Toolbox[135–137] and run using Matlab. Orientation and direction selectivity were calculated using the following equations for 1 – circular variance or 1 – circular variance in direction space, respectively, where $R(\theta_k)$ is the response to the angle θ_k[138,139]:

$$1 - \text{CirVar} = |\sum_k R(\theta_k)\exp(2i\theta_k)|/\sum_k R(\theta_k) \text{ and } 1 - \text{DirCirVar} = |\sum_k R(\theta_k)\exp(i\theta_k)|/\sum_k R(\theta_k)$$

Contrast responses were computed using the Nasha-Rushton fit function, where c is the contrast stimulus, R the output response of the neuron, A the maximum response of the neuron, c_{50} the contrast at which the response is halfway between baseline and maximum, n is the exponent, and s an additional parameter to allow the suppressive and excitatory exponents to vary at different rates[140–142]: $R(c; A, C_{50}, n, s) = A\, c^n/(c^{ns} + c_{50}^{ns})$

Spatial frequencies were calculated using a difference of Gaussians model for spatial frequency.[143,144] Temporal frequencies were computed using the following equation, where f is the temporal frequency, k a scaling constant, f_c the characteristic temporal frequency, f_h sets the corner frequency of the low-frequency limb of the function, and β sets the slope of the low-frequency limb[145]: $R(f) = k \exp(-f/f_c)^2 / (1 + (f_h/f)^\beta)$. The low pass index was computed by dividing the response at the lowest temporal frequency tested by the response at the preferred temporal frequency.

For intrinsic signal imaging to verify the location of cranial windows, we measured epifluorescence changes in the autofluorescence of mitochondrial flavoproteins in response to visual stimuli.[146] Visual stimuli consisted of sinusoidal rectangular gratings drifting along 8 orientations (0–180° at 22.5° intervals) at 1 spatial frequency (0.04 cpd) covering the whole height but only a quarter of the width of the HD monitor (1920 x 1080 pixels, i.e. each stimulus was 1920 x 480 pixels). Mice were facing the right edge of the monitor, so that all stimuli would correspond to different quarters of the visual field for the eye contralateral to the cranial window (left eye) and only the rightmost corner was visible to the ipsilateral eye. Stimuli were shown in a random order (including blank) for a duration of 15 s with 20 repetitions and were separated by 8s of blank screen. First, a picture was acquired with green light to visualize blood vessels as landmark and adjust the depth of the imaging plane. Flavoprotein autofluorescence was then excited with blue light (470 nm) measured through a green/red emission filter (ETX450/50, Chroma). Images were acquired using a CCD camera in macroscope configuration with 2 SLR camera lenses and LabView (NIH) as imaging software. Based on expected changes in autofluorescent signals after visual stimulation (weak positive signal followed by a stronger negative signal), stimulus response was computed as the mean of the frames acquired during the 5 s of stimulus presentation compared to the mean of the frames acquired during the last 3 s of the inter-stimulus interval and plotted in Matlab.

Ex vivo slice electrophysiology

Mice were anesthetized with isoflurane 75min after the end of the last behavioral session (hunting or mock) and then decapitated after toe-pinch check. Coronal slices (300 μm) containing V1b from both hemispheres were obtained using a Leica VT1200S vibratome. Slices were first transferred to an oxygenated chamber filled with choline solution (in mM: 110 Choline-Cl, 25 $NaHCO_3$, 11.6 Na-Ascorbate, 7 $MgCl_2$, 3.1 Na-Pyruvate, 2.5 KCl, 1.25NaH_2PO_4, and 0.5 $CaCl_2$, osmolarity adjusted to 310 mOsm with dextrose, pH 7.4) for recovery, and then incubated in oxygenated standard artificial cerebrospinal fluid (ACSF, in mM: 126 NaCl, 25 $NaHCO_3$, 3 KCl, 2 $CaCl_2$, 2 $MgSO_4$, 1 NaH_2PO_4, 0.5 Na-Ascorbate, osmolarity adjusted to 310 mOsm with dextrose, pH 7.4) and incubated for 40–60 minutes. Slices were used for electrophysiology 1–5 hours post slicing.

Slices containing V1b were placed on an Olympus BX51WI upright epifluorescence microscope equipped with infrared-DIC optics. V1b was identified as previously described.[147] Pyramidal neurons in L5 were visually targeted for whole-cell recordings using a 40x

Please cite this article in press as: Bissen et al., Ethological learning during the critical period resets synaptic setpoints in mouse binocular visual cortex, Neuron (2026), https://doi.org/10.1016/j.neuron.2026.06.016

water-immersion objective; visual identification was based on the teardrop shaped somata and the presence of an apical dendrite, and morphology was confirmed post hoc from biocytin fill reconstructions. Borosilicate glass pipettes with resistance between 4 to 6 MΩ were filled with K+ Gluconate-based internal solution (in mM: 100 K-gluconate, 10 KCl, 10 HEPES, 5.37 Biocytin, 0.5 EGTA, 10 Na-Phosphocreatine, 4 Mg-ATP, and 0.3 Na-GTP, osmolarity adjusted to 295 mOsm with sucrose, pH adjusted to 7.4 with KOH). All recordings were performed in slices that were superfused in oxygenated standard ACSF at 34 °C, using a Multiclamp 700B amplifier with a CV-7B headstage (Molecular Devices, Sunnyvale, CA). Data were passed through a 6 kHz Bessel low-pass filter and acquired at 10 kHz using a National Instruments Data Acquisition Board (DAQ, National Instruments, Woburn, MA) and an open-source MATLAB-based software WaveSurfer (HHMI Janelia, Ashburn VA).

To isolate mEPSC events, slices were superfused with standard ASCF containing a drug cocktail of tetrodotoxin (TTX, 0.1 μM), D-2-amino-5-phosphonovalerate (APV, 50 μM), and picrotoxin (25 μM). Pyramidal neurons were targeted and held at -70 mV in whole-cell voltage clamp, and neither series resistance nor liquid junction potential was corrected. Each neuron was recorded for 3–5 minutes in a series of 30s segments, and a 500 ms 5 mV hyperpolarizing voltage step was applied at the beginning of each segment to continuously monitor passive properties. Neurons were excluded if series resistance was > 20 MΩ, input resistance was < 70 MΩ, membrane potential was > -50 mV at break-in, or these properties changed by > 15% during the recording.

Immunostaining and confocal microscopy

Mice were deeply anesthetized using a ketamine/xylazine/acepromazine solution and perfused transcardially with ice-cold 0.01 M phosphate buffered saline (PBS) followed by 4 % paraformaldehyde (PFA) in 0.01M PBS (2–3 ml/min). After dissection and post-fixation in cold 4% PFA overnight followed by 3x 10 min PBS washes, brains were sectioned in 200μm thick slices to encompass complete dendritic trees and stored in 0.01M PBS at 4 °C until immunostaining. Selected slices with entire dendritic arborizations of L5 pyramidal neurons in V1b were permeabilized for 30 min in 0.4 % Triton X-100 in 0.01 M (PBST) and blocked for 60 min in blocking solution (2 % normal goat serum (NGS) in 0.4% PBST) at room temperature. Slices were then incubated with primary antibodies (see concentrations below) in blocking solution for 48–72h at 4 °C, washed 3x 10 min in PBS, and incubated with corresponding secondary antibodies for 2h at room temperature. Finally, slices were washed 3x 10 min in PBS, mounted using Fluoromount G and stored at 4°C until imaging.

This protocol was used for all imaging experiments on fixed tissues, except for cFos staining, where slices were directly incubated in blocking buffer (5% NGS, 3 BSA in 0.3% PBST) for 2h with no permeabilization step, and for which the incubation with secondary antibodies lasted 3h. Additionally, since PFA overfixation impairs somatostatin staining (Hajnalka Bokor, HUN-REN Hungary, personal communication and our own experience), brains collected to label dendritic inhibitory contacts were only post-fixed for 30 min after perfusion. Slices (200μm thick) were permeabilized for 30 min in 1% PBST, blocked for 30 min in blocking solution (10% NGS in 1% PBST), and processed as described above.

Slices used to assess spine density and morphology were stained with chicken anti-GFP (1:500) and rabbit anti-NeuN (1:500), followed by goat anti-chicken Alexa 488 and goat anti-rabbit Alexa 568 (both 1:500). Slices used to quantify perisomatic inhibitory contacts were stained with rabbit anti-GFP (1:500), chicken anti-parvalbumin (PV, 1:250) and mouse anti-Syt2 (1:250), followed by goat anti-rabbit Alexa 488, goat anti-chicken Alexa 568 and goat anti-mouse Alexa 647 (all at 1:500). Slices used to measure dendritic inhibition were stained with rat anti-SST (1:50), rabbit anti-VGAT (1:200) and chicken anti-GFP (1:500), followed by goat anti-chicken Alexa 488, goat anti-rabbit 647 and goat anti-rat 568 (all at 1:500). Slices used to quantify neuronal activity after DREADD expression were stained with rabbit anti-cFos (1:200), chicken anti-GFP (1:500), mouse anti-NeuN (1:500) and rat anti-mCherry (1:1000), followed by goat anti-rabbit Alexa 647, goat anti-mouse Alexa 405, goat anti-chicken Alexa 488 and goat anti-rat Alexa 568 (all 1:500). They were then imaged using a confocal laser scanning microscope (LSM 880, Zeiss), using the acquisition paradigm described below in the dedicated section on confocal image acquisition and analysis.

QUANTIFICATION AND STATISTICAL ANALYSIS

Behavioral analysis

Behavioral videos recorded during hunting/mock sessions were manually scored for: time of cricket dispensation into the arena, first orientation of the mouse to the cricket, start of the final (successful) attack, cricket capture, and end of cricket consumption. Time to capture (s) was then calculated as the time between cricket dispensation and capture, latency to attack (s) as the time between cricket dispensation and the start of the final attack, and attack duration (s) as the time between the start of the final attack and cricket capture. Further behavioral analysis was performed using DeepLabCut to estimate body part poses (DLC[57]). More than a hundred frames of hunting sessions were selected to represent a wide range of cricket and mouse positions and were manually labeled for the cricket as well as multiple points for the mouse head (nose, left and right ears, head center), body (middle of the body, left and right front and hindpaws) and tail (base, tip, and four intermediate points). These frames were used to train a ResNet-50 neural network. The performance of that network was evaluated using test data, and additional frames were selected and manually labeled to provide additional data to improve the performance of the network. Additional rounds of training were performed until the performance of the network was deemed sufficient. To calculate speed, DLC pose body parts with a confidence score below 0.82 were discarded. The position of the head for each frame was tracked using the four head labels described above. We calculated the instantaneous speed of each of these labels for each frame and applied a 30 frame window lowess smoothing function (MATLAB; locally weighted scatter

Please cite this article in press as: Bissen et al., Ethological learning during the critical period resets synaptic setpoints in mouse binocular visual cortex, Neuron (2026), https://doi.org/10.1016/j.neuron.2026.06.016

plot smoothing). The median of the output speeds was selected as the representative head speed for the animal at each frame. 6 total DLC poses were tracked to model the position of the tail. To calculate tail angle, we measured the angle formed by the last 3 tail poses (tail tip and closest 2 intermediate labels) for each frame.

Chronic spine imaging analysis

To minimize motion-induced artifacts inherent to awake imaging, images acquired using a resonant scanner at 15kHz were processed using two Matlab scripts (Mathworks, Natick, USA) kindly shared and modified by Benjamin Scholl (University of Colorado Denver, USA) or Kurt Sailor (Institut Pasteur, Paris, France). For the former, each dendritic segment was acquired as a Z-stack with each slice imaged 30 consecutive times and in-frame movement was corrected for each slice using non-rigid registration (NormCorrReg[148,149]). For the latter, each dendritic segment was imaged in 10 successive Z-stacks. Briefly, the mean image was calculated for each slice across all 10 stacks which was used as a template for rigid stack registration (MultiStackReg plugin, ImageJ, Fiji[150]) to correct for translational X-Y movement. Next, the 2D cross-correlation was calculated for each slice versus the mean slice image within the 10 stacks. A correlation threshold was then determined by the user to remove z-movement out-of-frame planes in the registered datasets. The corrected stack was reconstructed from averaging the remaining artifact-free Z-slices within the successive Z-stacks, followed by affine registration. This method removed movement artifact at the expense of a slight increase in image noise. Both codes are available on GitHub (see key resources table).

Spines were manually labeled across all time points in ImageJ (Fiji). Changes in spine density were quantified as a ratio of the spine density at each time point relative to the spine density at baseline (day 0). Spine formation or elimination was quantified as the number of spines added or lost at a given time point compared to the previous time point. Net spine change was calculated as the difference between the number spines added and lost at a given time point compared to the previous time point. Representative images were improved for clarity by removing signals from other cells using the mask function in Photoshop (Adobe).

Confocal image acquisition and analysis

Spine analysis

For large-scale, high-resolution imaging of spine density and morphology, L5 pyramidal neurons in V1b or widefield vertical (WF) cells in the superficial layers of the superior colliculus (SC) were imaged using an inverted confocal laser scanning microscope (LSM880, Zeiss). The localization of the pyramidal neurons in V1b or SC was confirmed with a 10x dry objective (NA 0.45) based on coordinates from the Allen Brain Atlas, and their identity confirmed morphologically.[72,151,152] The entire dendritic tree (SC) or apical, oblique or basal tree (V1) for each neuron was imaged using a 63x oil objective (NA 1.4) at 1024 x 1024 pixels (V1: pixel size of 220 x 200 x 300 nm (critical-period day 6; Day 6 + XPro) or 90 x 90 x 300 nm (day 1; adults); SC: 220 x 220 x 850nm). Stacks were deconvolved in Huygens (Scientific Volume Imaging) using the classic maximum likelihood estimation (CMLE) algorithm to improve resolution and signal to noise ratio. Apical dendrites were defined as located above the bifurcation of the primary apical dendrite (i.e. in the apical tuft), basal dendrites as arising directly from the soma, and oblique dendrites as arising from the primary apical dendrite and located at least 50μm from the soma. The entire dendritic trees and all spines were traced manually using the Filament Tracer module in Imaris (Oxford Instruments), with a diameter of 150 μm for spines and 150–300 μm for secondary and tertiary dendrites (see Video S1). Dendritic spine density (spine density per 10 μm of dendrite, for each dendrite) and spine head diameter (in μm) were obtained using the Statistics module in Imaris. In the representative images in Figures 3, 6, 7, and 8, signals from other nearby axons or dendrites were removed for clarity as follows: the selected dendrite was traced as a new filament in Imaris and used to reconstruct a surface with a low intensity threshold. This artificially enlarges the surface so that it becomes a cylinder encompassing the dendritic shaft and all the associated spines. All pixels outside of that surface were then set to 0 and in effect masked, leaving only the dendrite of interest.

Perisomatic inhibition

To study inhibitory contacts onto the somata of pyramidal cells or PV neurons, FP^+ or PV^+ somata in L5 from V1b were imaged using the Airyscan fast scanning and super-resolution module of a confocal microscope (LSM 880, Zeiss), respectively. Images were acquired as Z stacks (pixel size of 60 x 60 x 25 nm) using a 63x oil objective (NA 1.4) and deconvolved using the post-hoc processing algorithm of the Airyscan. The number of Syt2 contacts on FP^+ or PV^+ somata was first quantified using the Spots module in Imaris, which labels puncta based on an XY diameter provided by the experimenter. This diameter was estimated by measuring the average sizes of Syt2 puncta across multiple images and selected as 400nm for Syt2 contacts on FP^+ somata and 500nm for Syt2 contacts on PV^+ somata. Spots were manually removed if they appeared to belong to the same contact to avoid duplicate counting. Additionally, FP, PV and Syt2 signals were reconstructed using the Surface module in Imaris (Figure S3). To assess specifically Syt2 contacts on a given FP^+ or PV^+ soma, that soma was first reconstructed with a low surface resolution (surface grain size of 300nm) for the FP or PV channel, so that it would in effect be slightly larger than the soma itself by ∼ 1–2 μm (Figure S3B). This reconstruction served as a mask to automatically exclude all remote Syt2 signals, which are too far from the soma to represent an inhibitory contact, from subsequent analysis. If necessary, an inner FP or PV mask was also reconstructed with a high intensity threshold to faithfully recapitulate the shape of the soma and exclude somatic Syt2 signals (Figure S3C). This allowed the specific reconstruction and quantification of Syt2 staining at the surface of the FP^+ or PV^+ soma with a high resolution (surface grain size of 130nm and 110nm, respectively; Figures S3D–S3H). Finally, the volume and number of each Syt2 contact onto a FP^+ or PV^+ soma were obtained using the Statistics module in Imaris.

Please cite this article in press as: Bissen et al., Ethological learning during the critical period resets synaptic setpoints in mouse binocular visual cortex, Neuron (2026), https://doi.org/10.1016/j.neuron.2026.06.016

Dendritic inhibition

To study inhibitory contacts on the apical or basal dendritic trees of pyramidal neurons, L5 pyramidal neurons in V1b were imaged with the Zeiss LSM 880. The 10x air objective (NA 0.45) in conjunction with the Allen mouse coronal brain atlas were used to confirm the localization in V1b, and apical and basal dendritic arbors were imaged separately using the 63x oil objective (NA 1.4) as tiled Z-stacks (pixel size of 130 x 130 x 640 nm, 10% overlap for tiling using the bounding tile option). Tiled images were stitched and deconvolved in Huygens using the stitching module and the CMLE algorithm. The entire apical or basal dendritic arbor was manually traced in Imaris using the Filament Tracer module. To only include inhibitory puncta within $\sim$ 1–2 μm of the dendrite, a strategy similar to the quantification of perisomatic inhibition was used: a new channel was created based on the traced dendritic arbor, and used in the Surface module to generate a new surface with a low intensity threshold, in effect following closely the traced dendritic arbor, but with a slightly larger diameter ($\sim$ 1–2 μm). All voxels of all channels (i.e. YFP, SST, VGAT) outside this surface were then set to 0, so that only staining within that surface were used in subsequent analysis. From this masked channel following the dendrite, VGAT or SST signals were reconstructed based on a consistent intensity threshold using the Spots module. This allowed only VGAT and SST in close proximity to the dendrite to be included in the analysis. Furthermore, the number of colocalized SST and VGAT puncta was calculated using the Imaris "Colocalize Spots" extension with a threshold of 1.10 μm between the center of the puncta. The density of SST, VGAT and colocalized SST:VGAT puncta for each dendrite were finally obtained from the Statistics module.

cFos quantification

To measure neuronal activity in V1 upon DREADD expression, we quantified the number of neurons (identified by NeuN staining) that were also positive for the immediate early gene cFos as a proxy. To be representative of the whole region, four cortical slices per animal were selected across the antero-posterior axis. For each slice, one V1 was selected and L2/3 and L5/6 were imaged separately using the Zeiss LSM 880 with 20x air objective (NA 0.8), 1024 x 1024 pixels (pixel size of 420 x 420 x 500 nm). Both images were first stitched together using the pairwise stitching plugin with linear blend (Fiji) to facilitate identification of cortical layers, deconvolved in Huygens and analyzed in Imaris. Regions of interest (ROIs) of similar size (500 x 700 x 15 μm) were selected above L2/3 and L5/6 for each visual cortex and set in regions with bright DREADD expression (visualized by mCherry). The total number of c-Fos$^+$ and NeuN$^+$ cells within the ROI was automatically measured and manually confirmed using the Spots module based on a constant intensity threshold and XY diameter, both selected after careful estimation across multiple images throughout the dataset. The colocalization of cFos$^+$ and NeuN$^+$ puncta was subsequently performed using the "Colocalize spots" extension (distance threshold of 5 μm between the center of two puncta, based on average colocalization accuracy across multiple images) and extracted from the Statistics module. The ratio of active neurons in each layer of V1 was calculated as (number of cFos$^+$:NeuN$^+$ puncta/total number of NeuN$^+$ puncta) and plotted in GraphPad (Prism).

Intrinsic imaging analysis

To identify the position of cranial windows using intrinsic imaging, we took advantage of the retinotopic organization of the mouse primary visual cortex.[153] Visual receptive fields indeed elicit strong responses in patches of primary visual cortex, with adjacent fields producing responses in neighboring and overlapping patches. Receptive fields along the top-down and temporal-nasal axes of the visual field are represented in patches along the antero-posterior and medio-lateral axes of the primary visual cortex, respectively.[153] We thus presented four visual stimuli along the temporal-nasal axis of the visual field and analyzed the position of the responsive patches along the medio-lateral axis of the cranial window. Windows where the temporal-nasal axis matched the medio-lateral axis were defined as located above the primary visual cortex.

Calcium imaging analysis

Data analysis was performed using Suite2P[130] and Matlab (Mathworks). Timeseries acquired with a two-photon microscope were first registered and cells automatically identified in Suite2P (with default parameters), followed by manual addition or removal of cells as necessary in Suite2P. After Suite2p, a custom Matlab code (vhlab-TwoPhoton-matlab, available on GitHub) was used to compute the change in fluorescence ($\Delta F/F$) for each stimulus. The baseline was computed over the last 3 seconds of the inter-stimulus interval before each stimulus presentation, and the response was computed over the entire 5 second duration of the stimulus presentation. Tuning curves were subsequently calculated across all stimuli per receptive field property and the population average was computed using a custom nested analysis in Matlab (VH-Lab/vhtlab-mousehunting-matlab) to ensure an equal weight of all animals while including all imaged neurons. Representative images were prepared as the average of a timeseries with enhanced brightness and contrast in ImageJ (Fiji).

mEPSC recordings

Spontaneous mEPSC events were automatically detected using in-house scripts written with MATLAB as previously described.[154] Briefly, the script slides a mEPSC event-shaped template to identify putative mEPSC events, which were then passed through multiple quality control modules to exclude false-positives. To include events from distal dendrites in the upper layers, rise time cutoff for detection was set to 3 ms. Mean amplitude and frequency were first calculated for each 30 s recording segment, which were then averaged to generate the mean value for each cell. Rise time and decay time constants were calculated from the waveform average traces for each cell. Rise time is defined as the time for the current to increase from 10% to 90% of the peak amplitude. Decay time constant (τ) is derived from a first-order exponential fit of the decay phase. Cumulative distributions of

mEPSC amplitudes and inter-event intervals, as well as the average waveforms, were generated by randomly selecting and pooling 100 events from each cell.

Statistical analysis

Exact sample sizes, their definition (events, spines, dendrites, cells, animals) and statistical tests are all reported in the corresponding figure legend. Exact *p*-values are provided in Table S1, with statistical significance defined as a p-value below 0.05 and indicated as * for p 0.05, ** for $p < 0.01$, and *** for $p < 0.001$. Data plotting and analysis was performed in Prism (GraphPad) or using custom Matlab scripts (MathWorks; available on GitHub, see key resources table). Individual data points represent single animals for behavioral panels, single morphological units (mEPSCs, dendrites or spines) for cumulative distributions in structural and electrophysiological panels, and single neurons for nested analyses in structural and calcium imaging panels. Data are expressed as mean with error bars as standard error of the mean (SEM).

To assess significance levels, datasets were first tested for normality using Shapiro-Wilke's normality test. For normally distributed data, paired or non-paired t tests were used for one-way comparisons, and ANOVA with Tukey's correction was used for multiple comparisons. For non-normally distributed data, Wilcoxon's rank test was used for one-way comparisons, and a Mann-Whitney U-test was used for multiple comparisons. For regression analysis, a Pearson's correlation (for normally distributed data) was used. Cumulative distributions of electrophysiological and structural parameters were compared using a Kolmogorov-Smirnov test. Statistical tests and exact significant p-values are listed in Table S1.

To confirm that total cumulative distributions were not skewed by neurons with higher number of spines or inhibitory contacts, we selected an equal number of spines or inhibitory contacts per neuron using undersampling: for each neuron in a given group, we generated 100 random distributions using the smallest number of spines or contacts collected and calculated the median distribution, in which each neuron has equal weight; we then compared these median cumulative distributions for statistically significant differences using the Kolmogorov-Smirnov test. Results did not differ from those obtained using the full distributions, so full distributions were used.

For structural and calcium imaging experiments, as different animals contributed substantially different numbers of events (cells, dendrites, spines, inhibitory synapses), we performed a nested analysis with the Matlab function fitlme with the equation (in Wilkinson notation) $Y \sim 1 + TREATMENT + (1 \mid neuron)$ or $Y \sim 1 + TREATMENT + (1 \mid animal)$. This constructs a model of the effect of each treatment condition (mock vs hunting) with a normally-distributed free parameter for each neuron or animal to account for the fact that observations of multiple cells within a neuron or animal are not independent. This code is available on GitHub (VH-Lab/vhtlab-mousehunting-matlab). For structural experiments, we report both cumulative distributions (to show the shape of the data) and nested analysis (to account for the lack of independence of inhibitory puncta, spines or dendrites).

To quantify effect magnitudes across varying data structures, we selected the most appropriate calculations based on sample size and distributional assumptions. For parametric comparisons (including for post-hoc comparisons after ANOVA), Hedges' g was used for independent groups to correct for small-sample bias ($N < 20$), while Cohen's d_{av} was applied to paired data. For non-normally distributed data, we utilized non-parametric alternatives: the rank-biserial correlation (r) was reported for matched pairs, and the probability of superiority (PS; equivalent to the Area Under the ROC Curve) was used to characterize shifts in cumulative distributions. The PS represents the likelihood that a randomly selected observation from the experimental group exceeds one from the control group. Finally, for linear mixed-effects modeling, effect sizes were expressed via standardized beta coefficients (β) and an approximation of Cohen's d: Cohen's d was used to quantify the magnitude of difference between independent groups by normalizing the mean difference by the pooled standard deviation, while standardized beta coefficients represent the change in the dependent variable in units of standard deviation while accounting for random subject-level variance. The codes for all tests are available on GitHub (VH-Lab/vhtlab-mousehunting-matlab and turrigiano/CodeSpace/Bissen2025). The name of the test and corresponding coefficients are reported in the figure legends and Table S1.